

Sedimentology (2024) doi: 10.1111/sed.13211

# Tectono-sedimentary history of the upper Cedar Mountain Formation, Central Utah, USA

RYAN T. TUCKER\* (D), M. RYAN KING†, MICHAEL T. MOHR‡, RAY K. RENAUT\*, JAMES L. CROWLEY‡, JACK W. FEKETE§, PETER J. MAKOVICKY¶ and LINDSAY E. ZANNO\*\*'††

- \*Department of Earth Sciences, Stellenbosch University, Private Bag X1 Matieland, Stellenbosch 7602, South Africa (E-mail: tucker@sun.ac.za)
- †Natural and Environmental Sciences, Western Colorado University, 1 Western Way, Gunnison, CO 81231, USA
- ‡Department of Geosciences, Boise State University, Boise, ID 83725, USA
- §Department of Geosciences, University of Arkansas, Fayetteville, AR 72701, USA
- $\P Department\ of\ Earth\ and\ Environmental\ Sciences,\ University\ of\ Minnesota,\ Minneapolis,\ MN\ 55455,\ USA$
- \*\*Paleontology, North Carolina Museum of Natural Sciences, 11 W. Jones Street, Raleigh, NC 27601, USA
- ††Department of Biological Sciences, North Carolina State University, Campus Box 7617, Raleigh, NC 27695, USA

Associate Editor - Theresa Schwartz

### **ABSTRACT**

Current investigations into the Albian-Cenomanian sedimentary record within the Western Interior have identified multiple complex tectono-sedimentary process-response systems during the ongoing evolution of North America. One key sedimentary succession, the upper Cedar Mountain Formation (Short Canvon Member and Mussentuchit Member), has historically been linked to various regionally and continentally significant tectonic events, including Sevier foldand-thrust deformation. However, the linkage between the Short Canyon Member and active Sevier tectonism has been unclear due to a lack of high-precision age constraints. To establish temporal context, this study compares maximum depositional ages from detrital zircons recovered from the Short Canyon Member with that of a modified Bayesian age stratigraphic model (top-down) to infer that the Short Canyon Member was deposited at ca 100 Ma, penecontemporaneous with rejuvenated thrusting across Utah [Pavant (Pahvant), Iron Springs and Nebo thrusts]. These also indicate a short depositional hiatus with the lowermost portion of the overlying Mussentuchit Member. The Short Canyon Member and Mussentuchit Member preserve markedly different sedimentary successions, with the Short Canyon Member interpreted to be composed of paraautochthonous orogen-transverse (across the Sevier highlands) clastics deposited within a series of stacked distributive fluvial fans. Meanwhile, the muddy paralic Mussentuchit Member was a mix of orogen-transverse (Sevier highlands and Cordilleran Arc) and orogen-parallel basinal sediments and suspension settling fines within the developing collisional foredeep. However, the informally named last chance sandstone (middle sandstone of the Mussentuchit Member) is identified as an orogen-transverse sandy debris flow originating from the Sevier highlands, similar to the underlying Short Canyon Member. During this phase of landscape evolution, the Short Canyon Member - Mussentuchit Member depocentre was a sedimentary conduit system that would fertilize the Western Interior Seaway with ash-rich sediments. These volcaniclastic contributions, along

# 2 R. T. Tucker et al.

with penecontemporaneous deposits across the western coastal margin of the Western Interior Seaway, eventually would have lowered oxygen content and resulted in a contributing antecedent trigger for the Cenomanian–Turonian transition Oceanic Anoxic Event 2.

**Keywords** <sup>206</sup>Pb/<sup>238</sup>U Geochronology, Cenomanian, Cretaceous, Mussentuchit Member, Sevier fold-and-thrust belt, Short Canyon Member.

### INTRODUCTION

Ongoing investigations into the transition from Early to Late Cretaceous within North America, a period of geological and climatic change, are identifying an ever-increasingly complex, geological-based process-response system (Gulbranson et al., 2022; St. Pierre & Johnson, 2022; Tucker et al., 2022, 2023). For example, the formative study by St. Pierre & Johnson (2022) highlights the necessity for continued reexamination of classical models to explain North America's evolution during the Cretaceous. The Albian-Cenomanian upper Cedar Mountain Formation - namely the Short Canyon Member (SCM) and Mussentuchit Member (MM) - in the western San Rafael Swell of Utah, constitutes one of several crucial sedimentary successions deposited along the west coast of the epicontinental Western Interior Seaway (WIS) that preserves vestiges of ecological and environmental changes during global climatic fluctuations of the earliest Late Cretaceous (Fig. 1). Recent investigations of Mussentuchit Member strata have refined the understanding of palaeoenvironmental changes using a high-resolution geochronological framework of early Cenomanian transition between Oceanic Anoxic Event 1d (OAE1d) post-recovery phase and the onset of the Oceanic Anoxic Event 2 (OAE2) coupled with the Greenhorn Maximum Transgression (Zanno et al., 2019; Tucker et al., 2022, 2023; Renaut et al., 2023). Contemporaneous mid-Cretaceous volcanism and crustal shortening of the Western Interior during this time affected landscape evolution, with the most notable activity forming the Sevier fold-andthrust belt across Utah (Laskowski et al., 2013; Quick et al., 2020). A recently improved temporal framework for the Mussentuchit Member (Tucker et al., 2023) now offers the opportunity to reconsider linkages between regional tectonic processes and sedimentary responses.

Historically, researchers have associated tectonically-driven landscape evolution with the deposition of the Cedar Mountain Formation (Heller *et al.*, 1988; Heller & Paola, 1989;

Stikes, 2007; Suarez et al., 2014; Kirkland et al., 2016). Currie (2002) and Suarez et al. (2014) identified the occurrence of a transition from distal foredeep-proximal backbulge to foredeep within the upper Ruby Ranch Member of the middle Cedar Mountain Formation, central Utah, which has age estimates spanning from ca 120 to ca 106-103 Ma that partially coincide with the emplacement of the Canyon Range thrust (145–110 Ma) to the west (Currie, 2002; DeCelles & Coogan, 2006; Suarez et al., 2014; Yonkee & Weil, 2015; Di Fiori et al., 2020; Tucker et al., 2020; Lee, 2021). Development of the Canvon Range thrust would have significant regional cascading effects both geologically and biologically (Caldwell, 1984; DeCelles, 2004; Oboh-Ikuenobe et al., 2008; Bhattacharva & MacEachern, 2009; Haq, 2014; DeCelles & Graham, 2015; Eldrett et al., 2015; Slattery et al., 2015; Schwartz et al., 2021). Increased subduction rates during the Albian-Cenomanian transition intensified volcanism across the arc and shortening across the fold belt, which reactivated the Sevier foldand-thrust belt (Currie, 2002; DeCelles & Coogan, 2006; Laskowski et al., 2013). As a result of the above tectonism, the foredeep migrated farther east, resulting in the emplacement of the overlying Short Canvon and Mussentuchit members of the Cedar Mountain Formation in the foredeep, adjacent to the Pavant Thrust zone in the earliest Cenomanian (DeCelles & Coogan, 2006; Laskowski et al., 2013; Suarez et al., 2014; Tucker et al., 2023).

Despite the recent increased understanding of these events, high-resolution chronostratigraphic linkages to key regional tectonic palaeogeographical landmarks remain tenuous. Although most of the latest work has focused on the Mussentuchit Member, the authors were also comsimultaneously pelled to reconsider underlying Short Canyon Member (Kirkland et al., 2016). The Short Canyon Member is a northward thickening clastic wedge sandwiched between the Ruby Ranch and Mussentuchit members, first identified by Kirkland & Madsen (2007) and initially named the Moore Road Conglomerate. Subsequently, Doelling

13633091, 0, Downloaded from https://onlinelibrary.wiley.com/doi/10.1111/sed.13211 by Stellenbosch University, Wiley Online Library on [04/07/2024]. See the Terms

and Conditions (https://onlinelibrary.wiley.com/terms-and-conditions) on Wiley Online Library for rules of use; OA articles are governed by the applicable Creative Commons

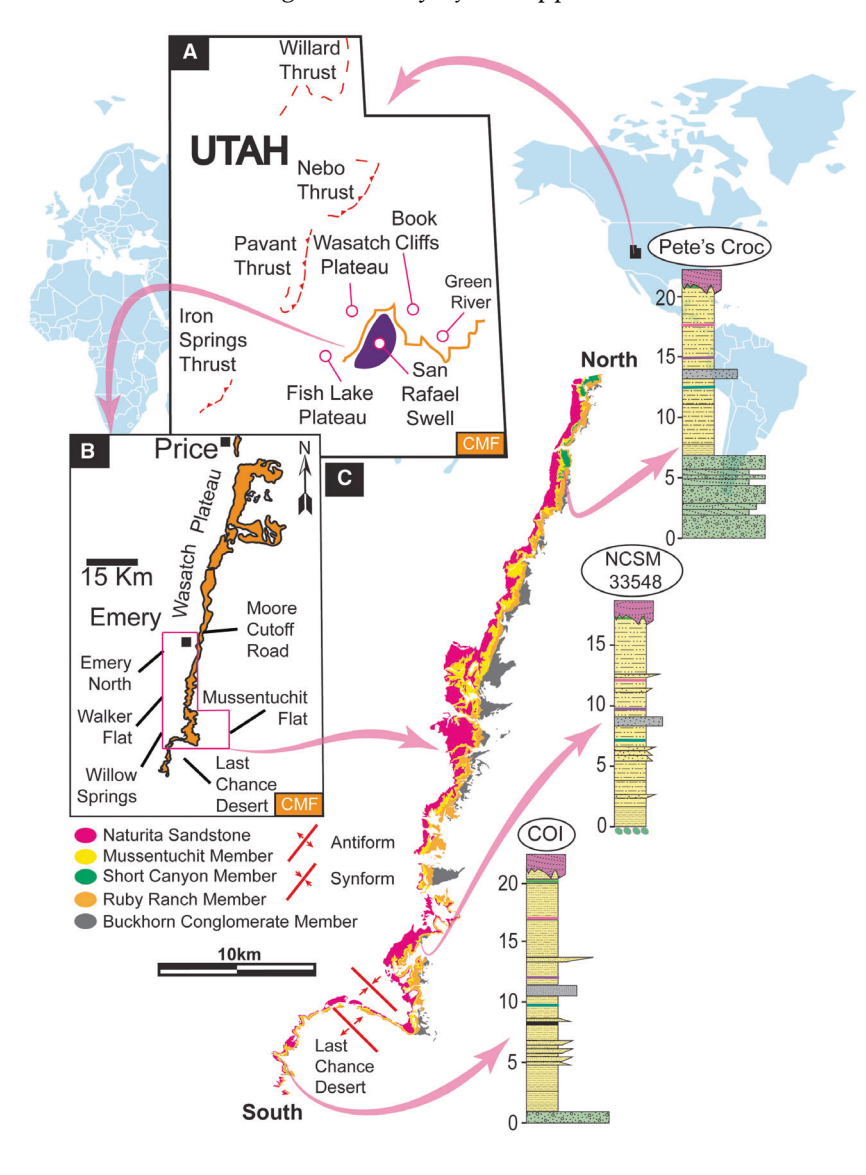


Fig. 1. Location map of exposed Cedar Mountain Formation (CMF) across central and east central Utah, modified from Sprinkel et al. (1999), Hintze et al. (2000) and Tucker et al. (2020, 2022, 2023). (A) Regional map with 1: 24 000 (7.5-min) quadrangles. (B) Exposed units of the Cedar Mountain Formation and overlying Naturita Formation, along with an inset highlighting outcrop of the Short Canyon Member near the Last Chance Desert. (C) Selected stratigraphic sections (COI - Cliffs of Insanity; NCSM 33548; and Pete's Croc locality just south of the Moore Cutoff Road) of the outcropping Short Canvon and Mussentuchit members, see Tucker et al. (2022, 2023) for additional stratigraphic location for each.

Kuehne (2013) presented an updated lithostratigraphic description naming the unit as the Short Canyon Member and identified a type section. During recent surveys in the region between Moore Cutoff Road and Last Chance Desert (east of the Wasatch Plateau), continuous exposures were observed of the Short Canyon Member ranging from a pebble lag in the Mussentuchit Wash to a southward thickening bedded conglomerate near the Last Chance Desert (Tucker et al., 2022).

Additionally, above the Short Canyon Member, within the middle Mussentuchit Member lies an atypical, stratigraphically extensive sandy unit, which informally divides the Mussentuchit Member into lower and upper units; herein, informally named the last chance

sandstone (Tucker et al., 2020, 2022, 2023). This regionally extensive sandstone interval commonly contains reworked fossil material (vertebrate microfossils and eggshells) and lacks suspension-settling silts and clays (other than clay rip-ups). Clastic conglomerates of the Buckhorn Conglomerate and Short Canyon Member have been historically linked to thrust-related events in the Sevier fold-and-thrust belt, which potentially can also be ascribed to the newly identified last chance sandstone (Kirkland et al., 1997: Kirkland & Madsen, 2007: Lawton et al., 2010; Hunt et al., 2011). Due to the revision of previously published geochronological data relating to the Mussentuchit Member (Tucker et al., 2023), it is now tenable to reliably calibrate subduction-related arc volcanism processes

# 4 R. T. Tucker et al.

to multiple effects, not limited to: (i) contractional deformation in the adjacent Pavant thrust and sediment unloading; (ii) flexural responses in the foredeep (Mussentuchit depocentre); and (ii) resulting transgression–regression sequences in the adjacent Western Interior Seaway.

To test this paradigm, this manuscript aims to contextualize the tectono-sedimentary relationship between regional and continental-scale events with sedimentary successions of the upper Cedar Mountain Formation north of the Fish Lake Plateau and south-east of the Wasatch Plateau along the San Rafael Swell (Fig. 1B). In doing so, the following geological information is provided: (i) detailed facies descriptions of the Short Canyon Member and last chance sandstone (Mussentuchit Member); (ii) local to regional tectonically linked sedimentary history; (iii) new correlations to key units in the hinterland along with regional transgression and regression cycles found elsewhere in the WIS: and (iv) novel chronostratigraphic linkages across the Western Interior. These new data refine tectono-sedimentary and lithostratigraphic linkages during the transition into the earliest Late Cretaceous in central Utah and the Western Interior.

# GEOLOGICAL BACKGROUND

Initially developed as a foreland basin, the Western Interior was partitioned into a mosaic of younsub-basins related to Jurassic-Eocene orogenesis (155-35 Ma), which reflects deformation associated with the thin-skinned Sevier fold-and-thrust belt and subsequent Laradeformation (Willis. 1999: Roca Nadon, 2007; Laskowski et al., 2013; Yonkee & Weil, 2015; Herring et al., 2016; Giallorenzo et al., 2018). Key to this study is the proposed temporal relationship between the Pavant Thrust and flexural subsidence in the Sevier fold-and-thrust belt (Fig. 2B) (Currie, 2002). The ongoing migration of the forebulge and foredeep caused the deposition of the lower Cedar Mountain Formation to occur eastward of the crustal forebulge. In contrast, the uppermost Cedar Mountain Formation (Mussentuchit Member) was deposited in the eastern part of either a retroarc foredeep or collisional foredeep following passage of the forebulge (Currie, 1997, 2002; Eberth et al., 2006; Miall & Catuneanu, 2019; Hildebrand & Whalen, 2021a,b; Hildebrand et al., 2022; Lowey, 2023).

Sedimentary successions of the upper Cedar Mountain Formation deposited in the developing foredeep, namely the Short Canyon Member and the Mussentuchit Member, have been qualitatively linked to thrusting to the west and sea-level fluctuations to the east (Fig. 2A and B) (Sprinkel et al., 1999; Hunt et al., 2011; Doelling & Kuehne, 2013; Kirkland et al., 2016; Tucker et al., 2020, 2022). The thrust events to the west of the basin have been corroborated by the extensive of DeCelles (2004) and Laskowski et al. (2013) who demonstrated the strong relationship between exhumed terrains in the Pavant Phase of the Sevier fold-and-thrust belt and recovered detrital zircon age spectra in the adjacent foreland basin (DeCelles, 2004; DeCelles & Coogan, 2006; Schwartz et al., 2021; Singer et al., 2021). This phase of Sevier foreland development was synchronous with 'Phase C' of volcanic activity in the western Cordilleran Magmatic Arc (Yingling & Heller, 1992; DeCelles et al., 1995) and a period of voluminous volcanic activity coeval with the Peninsular Ranges Orogeny (DeCelles & Graham, 2015, p. 501; Tucker et al., 2020; Hildebrand & Whalen, 2021b, Hildebrand et al., 2022). More regionally, two critical studies by Pujols et al. (2020) and Quick et al. (2020) indicate that the Sevier fold-and-thrust belt, namely the Nebo (100.7  $\pm$  2.2 Ma), Pavant and Iron Spring  $(100.18 \pm 0.04 \text{ Ma})$  thrusts, reactivated nearsynchronously across much of Utah during the transition from the Albian to Cenomanian (Fig. 2A). However, a chronostratigraphic framework necessary to firmly tie synorogenic deposition of the Cedar Mountain Formation to emplacement of the Pavant thrust sheet has not existed before this study. The precedent for this linkage is supported by the results of Hunt et al. (2011) who identified the source for Short Canvon Member clastics to be from Ordovician to Devonian rocks in the western Sevier fold-andthrust belt along central Utah, but deemed the Short Canyon Member to be independent of the westerly San Pitch Formation in the adjacent foredeep (see Chronofacies B, Hunt et al., 2011, p. 202). Exposed sedimentary successions of the Cedar Mountain Formation occur east-central and central Utah (Kirkland et al., 2016). The Cedar Mountain Formation in the San Rafael Swell includes six regionally variable members (in stratigraphic order): (i) Buckhorn Conglomerate Member; (ii) Yellow Cat Member; (iii) Poison Strip Sandstone Member; (iv) Ruby Ranch Member; (v) Short Canyon Member; and (vi) Mussentuchit Member (Kirkland & Madsen, 2007; Hunt et al., 2011; Doelling & Kuehne, 2013; Kirkland et al., 2016) (Figs 1C and 2C). Individual members are laterally

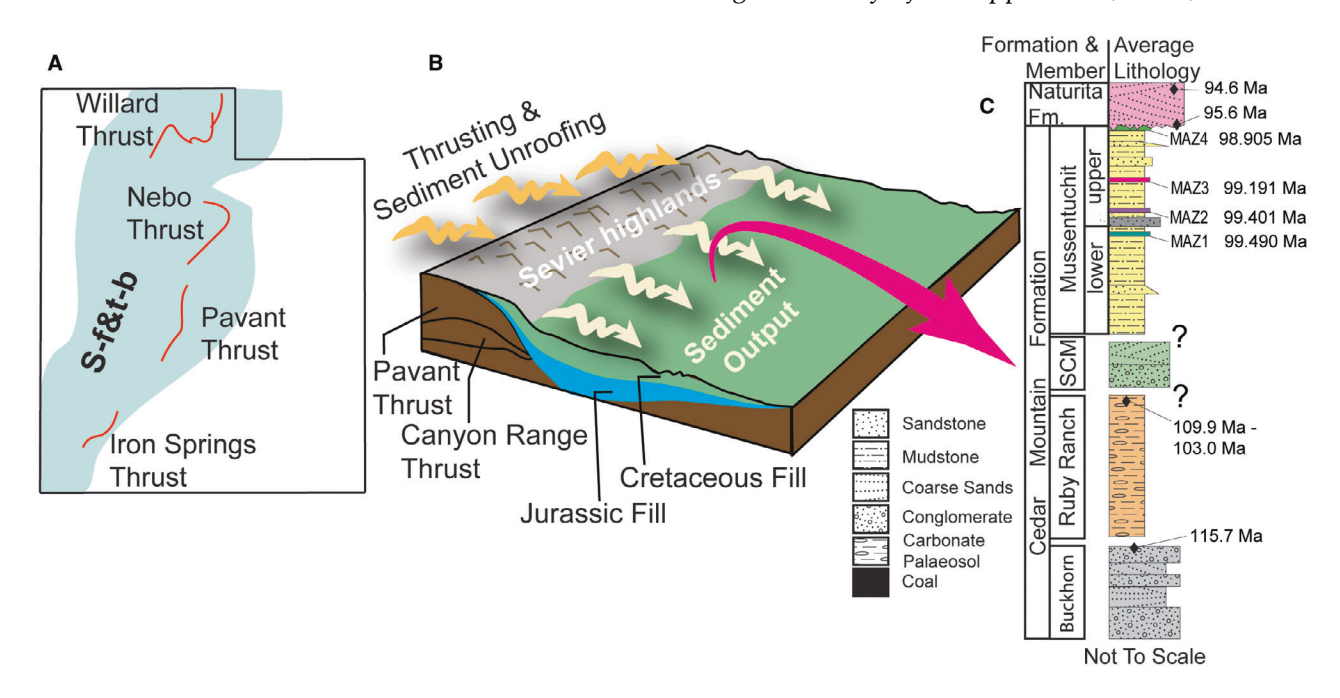


Fig. 2. From left to right: (A) location of the study area in central Utah with relation to the southern Iron Springs and Northern Nebo thrusts across the Sevier fold-and-thrust belt (SF&TB); (B) structural reconstruction highlights the Jurassic–Cretaceous sedimentation within the evolving foredeep; and (C) generalized stratigraphic section of the Cedar Mountain Formation (Buckhorn Conglomerate, Ruby Ranch, Short Canyon and Mussentuchit members) within the westernmost portions with age data based on Tucker *et al.* (2020, 2023) and Renaut *et al.* (2023). Modified from Kirkland *et al.* (2016) and Tucker *et al.* (2020, 2022).

discontinuous and thus not always present (Kirkland *et al.*, 2016). This investigation focused on deposits along the western corridor (central Utah) just east of the Wasatch and Fish Lake plateaus, with only the Buckhorn Conglomerate, Ruby Ranch and Mussentuchit members consistently present, along with minor exposure of the Short Canyon Member (Figs 1C and 2C).

The type section for the Short Canyon (Moore, Utah) is geographically located in the Molen Reef area of the San Rafael Swell north of I-70, designated by Kirkland & Madsen (2007) and Doelling & Kuehne (2013). Doelling & Kuehne (2013) describe the Short Canyon Member as a distinctive, three-part conglomerate bed with interbedded sands and muds. Clastics have been identified as sub-angular to rounded Ordovician Devonian Eureka quartzites, limestone and interbedded to intercalated coarse sandstones, with siliciclastics likely derived from the westerly adjacent Sevier fold-and-thrust belt (i.e. Sevier highlands) (Hunt et al., 2011; Doelling & Kuehne, 2013; Kirkland et al., 2016). Palaeoenvironmental reconstructions for the Short Canyon Member indicate fluvially influenced alluvial deposits (Hunt et*al.*, **2011**; Doelling

Kuehne, 2013). On the other hand, exposed sections of the Mussentuchit Member along the western San Rafael Swell are composed of volcanilithic-rich (smectitic clays) bentonites and alternating drab-grey to light-grey silty-mudstones and muddy-siltstones (Stokes, 1952; Kirkland et al., 1997, 1999, 2016; Garrison Jr. et al., 2007; Tucker et al., 2020, 2022). Facies analysis and architectural reconstruction by Tucker et al. (2022) of sediment successions preserved within the Mussentuchit Member suggest deposition within a broad sweeping plain influenced by both distal alluvial (floodplain) and backshore processes (up-dip delta plain/coastal). Locally, in Mussentuchit Wash, the Mussentuchit Member is laterally continuous throughout the study area and is typically ca 22.0 to 30.0 m in total thickness (Fig. 2).

# Chronostratigraphic background

Ongoing efforts to refine chronostratigraphic frameworks for sedimentary units within the Cedar Mountain Formation have improved our understanding of these strata in time and space (Fig. 3). Work within the lower Ruby Ranch Member indicated deposition coeval with the last

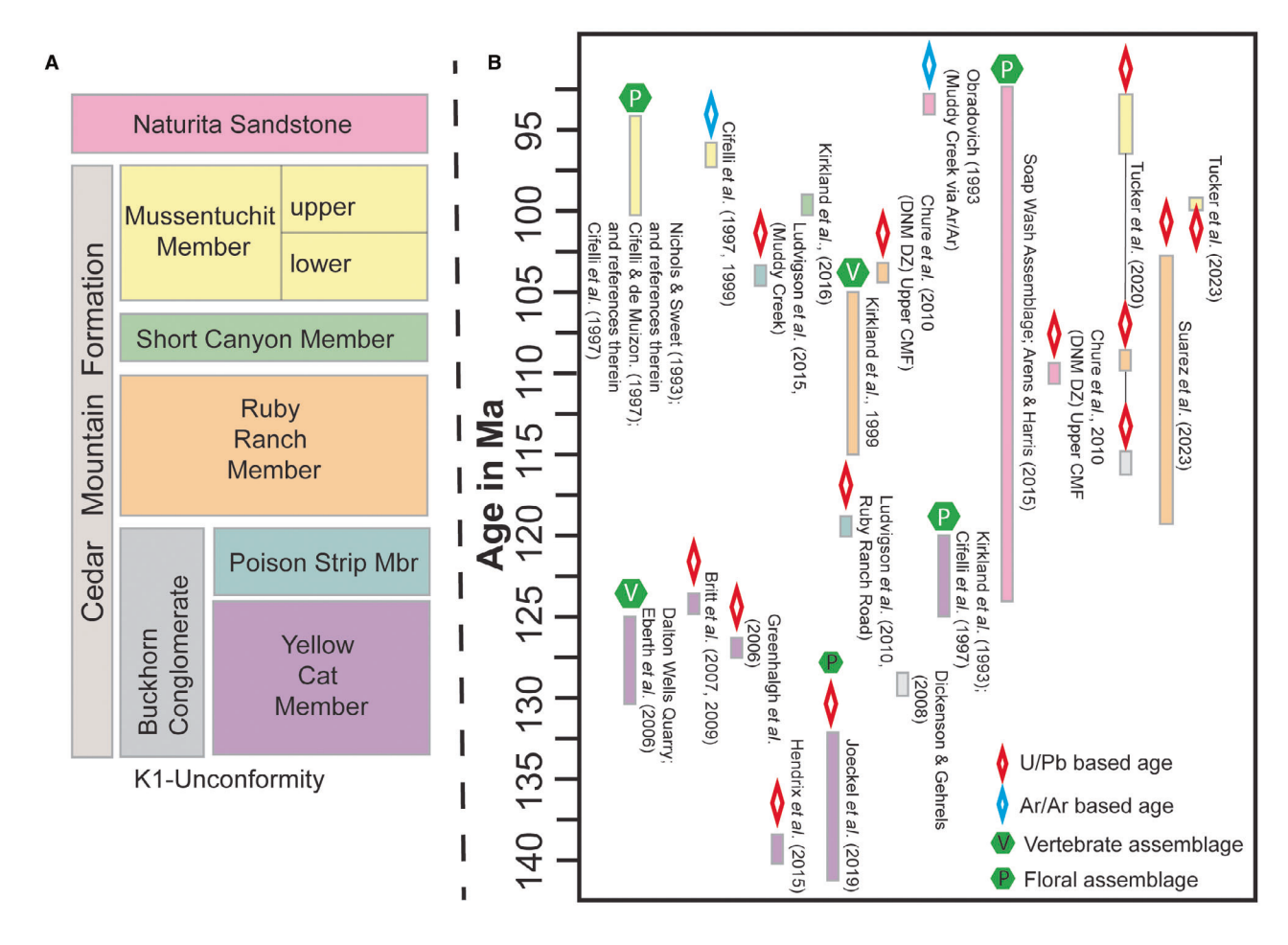


Fig. 3. (A) Simplified stratigraphic column of all currently recognized members of the Cedar Mountain Formation, geographical maps based on Kirkland *et al.* (2016) and Tucker *et al.* (2020, 2022). (B) Modified and updated from Tucker *et al.* (2020). Previous published temporal placement of stratigraphic units within the Cedar Mountain Formation, including but not limited to: the Buckhorn Conglomerate, Upper and Lower Yellow Cat Member, Poison Strip Member, Ruby Ranch Member, Short Canyon Member, Mussentuchit Member, along with the overlying Naturita Sandstone, with data recovered from Bhattacharya & MacEachern (2009); Dickinson & Gehrels (2008); Blakey (2014); Elderbak *et al.* (2014); Suarez *et al.* (2014); Ludvigson *et al.* (2015); Lockshin *et al.* (2017); Shang *et al.* (2018); Joeckel *et al.* (2019); Tucker *et al.* (2020); Renaut *et al.* (2023); Suarez *et al.* (2023); Tucker *et al.* (2023).

pulses of unroofing of the Canyon Range thrust, and the upper Ruby Ranch Member possibly coincided with the earliest phases of Pavant thrusting, both to the west in the Sevier fold-and-thrust belt (Cretaceous Sevier highlands) (DeCelles & Coogan, 2006; Hunt et al., 2011; Hunt, 2015; Forster, 2022; Suarez et al., 2023). The most recent U–Pb geochronology of zircon coupled with carbon isotope records indicate a depositional range for the Ruby Ranch Member spanning from 120 to 106–103 Ma and a specific age for depositional localities such as Lake Carpenter at 115  $\pm$  0.14 Ma (Fig. 3) (Ludvigson et al., 2015). This corroborates earlier estimates made via: (i) U–Pb

dating via chemical abrasion—isotope dilution—thermal ionization mass spectrometry (ID-TIMS) of tephra zircon recovered at the contact of the Buckhorn Conglomerate and Ruby Ranch Member at  $103.7 \pm 2.6$  Ma by Ludvigson  $et\ al.\ (2015)$ ; and (ii) laser ablation—inductively coupled—mass spectrometry (LA-ICP-MS) U–Pb dating of detrital zircons recovered from the upper Ruby Ranch Member, with a  $110.1 \pm 4.5$  Ma maximum depositional age (MDA) (Tucker  $et\ al.,\ 2020$ ). The upper Ruby Ranch Member could be as young as  $ca\ 106$ –103 Ma, confirming Albian emplacement and strengthening linkages to the terminal Canyon Range thrust and the earliest phases of

Pavant thrusting to the west (Ludvigson et al., 2015; Tucker et al., 2020). Until now, without an age constraint from radioisotope geochronology, the age interpretation of the Short Canyon Member has relied on the overlying Mussentuchit Member for temporal context. Early work by Cifelli et al. (1997, 1999) dated the Mussentuchit Member at  $98.39 \pm 0.07$  Ma using  $^{40}\text{Ar}/^{39}\text{Ar}$ dating of sanidine phenocrysts (recovered from horizon). corroborating the previous estimates of ca 98.5 Ma (Obradovich, 1993) and  $98.9 \pm 0.6$  Ma (Gradstein et al., 1995). Subsequent plagioclase 40Ar/39Ar dating (recovered from bentonitic muds) by Garrison Jr. et al. (2007) indicated an age of 97.0  $\pm$  0.1 Ma and LA-ICP-MS U-Pb dating of detrital zircon by Tucker et al. (2020) indicated that deposition occurred between ca 96 Ma and ca 94 Ma. Most recently, Tucker et al. (2023) presented high-precision CA-ID-TIMS U-Pb zircon dates for four primary ash beds preserved in the Mussentuchit Member (herein noted as Mussentuchit Ash Zones 1-4, MAZ1-MAZ4, see Tucker et al., 2023), and the resulting ages (interpreted through Bayesian age modelling) indicated that deposition occurred between 99.674 + 0.439/-0.176 and 98.905 + 0.158/-0.183 Ma (Fig. 3). Based on the synopsis above, the deposition of the Short Canyon Member is suspected to have initiated around ca 109 Ma, and perhaps as late as ca 103 Ma, and continued until 99.7 Ma, extending across the Albian-Cenomanian transition, in agreement with Hunt et al. (2011) and Kirkland et al. (2016).

#### **METHODS**

Ongoing fieldwork (as described in Tucker et al., 2022) includes detailed facies and architectural element analysis, following the framework established and revised by Miall (2014), along with additional influence by Neves et al. (2005), Roberts (2007) and Tucker et al. (2017, 2022), with stratigraphic sections measured via Jacob staff and Brunton compass at decimetre scale. The same sedimentological techniques were employed for consistency between studies and utilized a uniform set of facies codes best used to describe the outcrop sections (Tucker et al., 2022). Stratigraphic sections and correlations are described according to the geographic occurrence in the 7.5-min (1:24 000) quadrangle topographic map series across the study area (Fig. 1).

Isotopic classification and identification analysis of volcaniclastic samples via X-Ray Diffraction

(XRD) were completed by Dr. Sabine Verryn at XRD Analytical and Consulting CC, Pretoria, South Africa. Micronization of four of the fifteen samples collected, one representative of each ash layer (MAZ1 - Burnt Leg; MAZ2 - Ash Hole; MAZ3 - Ash Hole; MAZ4 - VAMP), was performed in a McCrone micronizing mill (The McCrone Group, Westmont, IL, USA) and the backloading method was used in the preparation of these samples (Kleeberg et al., 2008). The four samples were analysed using a Malvern Panalytical Aeris Minerals diffractometer (Malvern Panalytical, Malvern, UK) with PIXcel detector and fixed slits with Fe-filtered Co-Kα radiation. The samples were scanned at room temperature within a range of 10 to 80 °2θ and a step size of 0.02 °2θ, with measurement times varying between 5 and 10 min per scan. The phases were identified using X'Pert HighScore, and the data were assessed with the software package High-Score Plus version 4.9 (HighScore Plus software version 4.9, PANalytical B.V., Almelo, The Netherlands). Comparative phase amounts (weight %) were estimated using the Rietveld method and flux-free of trace elements and rare earth elements (REEs). As the Rietveld method was used to estimate comparative phase amounts, no standards or monitors were used in this analysis.

All of the fine-grained volcanic ash samples were milled and geochemically analysed at the Central Analytical Facilities (CAF) at Stellenbosch University, South Africa. To prepare samples for major and minor trace element analyses, the samples were milled using a tungsten-carbide Zibb mill. Primary elemental composition of the ashes was performed via X-ray Fluorescence (XRF) Spectroscopy using a PANalytical Axios Wavelength Dispersive spectrometer installed with a 2.4 kW rhodium tube and using the following four analytical crystals: LIF200, LIF220, PE 002, Ge 111 and PX1. Fused glass disks used for this analysis were produced by combining 7 g of high-purity trace element and rare earth element-free flux (LiBO<sub>2</sub> = 32.83%,  $\text{Li}_2\text{B}_4\text{O}_7 = 66.67\%$ , LiI = 0.50%) and 0.7 g of the ash sample. The subsequent fusing of this mixture was completed in platinum crucibles with Claisse® M4 gas fluxer at 1100-1200°C. The following control standards were used to calibrate the results obtained: NIM-G, BE-N, JB-1, HUSG-1 and BHVO-1. A Resolution 193 nm Excimer laser from Applied Spectra (West Sacramento, CA, USA) connected to an Agilent 7700 Q ICP-MS or 8800 QQQ ICP-MS (Agilent Technologies, Santa Clara, CA, USA) was used to complete a trace and

# 8 R. T. Tucker et al.

rare earth elements (REE) analysis by laser ablation-inductively coupled-mass spectrometry (LA-ICP-MS). The method presented Eggins (2003) was utilized for this analysis, and accuracy was verified during LA-ICP-MS by simultaneously analysing a fusion control standard (BCR-2, values from Jochum et al., 2011). The software package LADR, from Norris Scientific (Norris & Danyushevsky, 2018) was used to process the data obtained from the LA-ICP-MS analysis. The SiO<sub>2</sub> content obtained for each ash sample analysed via XRF analysis was used as the internal standard (Longerich et al., 1996). The Igpet modelling software was used to construct the discriminant diagrams of the major and minor trace element data collected from the sampled volcanic ash. Major and minor element data analysed across all ash horizons for the Mussentuchit Member occurred within the  $1\sigma$  level of confidence.

Sample MC-07 was collected from the Short Canyon Member of the Cedar Mountain Formation at the Moore Cutoff section for detrital zircon geochronology (GPS provided in File S1). The collection comprised approximately 2 kg of upper medium to coarse-grained sandstone for heavy mineral separation. The rock sample was first disaggregated using a jaw crusher and disc mill before removing the fine fraction. The denser fraction was concentrated using a Blue Bowl Centrifugal Concentrator. Grains with magnetic susceptibility (0.5 A, 1.0 A and 1.5 A) were removed using a Frantz Magnetic Separator (S.G. Frantz Co., Tullytown, PA, USA). A final zircon fraction was obtained by heavy liquid separation using methylene iodide (3.32 g/cm<sup>3</sup>), which was then split into unbiased and handpicked zircon aliquots. Zircons with euhedral morphologies were picked to improve the likelihood of encountering syndepositional zircon grains [Cathodoluminescence (CL) images with File S2]. Hand-picked zircon grains were sent to the Boise State University Isotope Geology Laboratory for detrital zircon U-Pb age screening via LA-ICP-MS. For a complete description of the analytical methods used, please see File S3. The voungest grains found during LA-ICP-MS screening were subsequently analysed via chemical abrasion-isotope dilution-thermal ionization mass spectrometry (CA-ID-TIMS) for high-precision dates (sampling and results for LA-ICP-MS are within File S4 and CA-ID-TIMS File S5). For all previous LA-ICP-MS and CA-ID-TIMS data and results, see Tucker et al. (2023; online data repository A-G).

### RESULTS

# Sedimentology

Within the Short Canvon Member, twelve lithosomes were identified (Table 1), along with four repeatedly occurring architectural elements (Table 2), which were combined to identify meaningful sedimentary facies (F) (Table 3). Additionally, lithological details are provided to infer the depositional history of the last chance sandstone of the middle Mussentuchit Member (described by Tucker et al., 2022, 2023). For each weathered and unweathered colour, codes are presented in Table 4 (Color, 2011). Upper and lower bounding surfaces range between first and seventh-order and are based on terminology from Vail et al. (1977) and Miall (2010) (Table 5). For detailed facies descriptions of the Mussentuchit Member, please see Tucker et al. (2022).

# Facies Association 1 (FA1)

Facies Association 1 (FA1), limited to the Short Canyon Member, is composed of lithosomes Gcb, GSe, Gmx, Gmm, Gst, Gsp, St, Si, Sm, Ss and Sh. In outcrop, FA1 is typically grey and weathered to light orange, light red, light brown, orange and light black (Figs 3, 4 and 5). Along with varied clastics (boulders and cobbles) and coarse sands, FA1 contains sand-silt but impoverished of clays (Fig. 6). FA1 exhibits seventh-order erosive lower-bounding surfaces and fourth to sixth-order upper-bounding surfaces. Beds ranging from <0.1 to 4.0 m are found near the type section and, if stacked, can be up to 10 to 12 m thick (Doelling & Kuehne, 2013). Clastic-rich units can be crudely bedded, lenticular to sheet-like, typically individual beds exhibited non-grading to normal grading, and composed of coarse sands, granules, pebbles, cobbles and boulders (typically impoverished of clay fractions). Although crude, sheet-like geometry is frequent, a few clastic-rich units preserve trough-cross bedding or channelization (Gst and Gsp). Laterally, FA1 gravels can extend tens to hundreds of metres, and these beds occur at the same stratigraphic interval for 10 to 20 km along the outcrop belt (Figs 4 and 5A). Internally, clasts range from sub-angular to rounded, clastsupported to matrix-supported, polymictic to oligomictic (GSe and Gmx), with many clasts identified as quartzites, siliceous limestone, sandstones and infrequent cherts. Architecturally, FA1 gravels can present as crude concave-up channels (CH) that are low-angled planar cross-bedded with basal rip-ups and gravel lags (LA), and

**Table 1.** Lithosome codes identified in the Mussentuchit Member of the upper Cedar Mountain Formation, modified from Roberts (2007), Miall (2014) and Tucker *et al.* (2022).

Facies code	Grain scale	Sedimentary structure	Interpretation
Gmm	Massive, matrix-supported gravels	Grading-non, normal, reverse	Mass flow
Gcb	Massive, largely clast-supported	Normal grading	Mass flow
Gmx	Basal gravel rip-ups	Erosional surface, basal gravels	Scouring flow with rip-up clasts, waxing energies
Gst	Gravel, stratified	Trough cross-bedding	Fluvial in-channel flow
Gsp	Gravel	Planar cross-bedding	Channel migration
GSe	Gravel with sand	Crude cross-bedding	Mass flow
Sm	Sandy, with or without mud	Massive, void	Void
Sh	Sandy–silty, with or without mud	Planar lamination	Plane-bed flow
Ss	Sandy–silty, with or without mud	Broad shallow scours	Scour fill
St	Sandy–silty, with or without mud	Troughs	Channel flow with sand upbuilding
Si	Sandy–silty, with or without mud	Low-angle cross-bedding	Scour fills
Sp	Coarse sand, sand, silt	Planar cross-bedding	Lateral accretion

**Table 2.** Architectural elements (lithosomes) identified in the Mussentuchit Member.

Element	Symbol	Facies	Geometry
Channels	СН	Any Combination	Sheet, concave-up erosional base, commonly bounded by third to fifth-order surfaces
Lateral Accretion	LA	Gmx, Ss, Sm, Si	Wedge with moderately angled internal planar cross-stratification
Scour Hollow	НО	Gmx, Sm, Ss	Scoured troughs
Gravel Bars	GB	Gmm, Gsp, Gst	Poorly stratified medial and lateral gravel bars

laterally discontinuous large-scale lenticular to wedge-shaped gravel bars (GB), which typically grade to granules, and coarse sand units, lacking imbrication, and periodically indicate finingupward (Figs 4, 5B, 5C, 5F and 6). Individual sand-silt bodies typically preserve: (i) trough cross-stratification (St and Sp) that is commonly 0.3 to 3.0 m thick (angle of repose commonly ranges between 8° and 26°); or (ii) planar crossstratification (Sr, Sh and Ss) with inclinations of 10° to 18° (Figs 4, 5B, 5D and 6). FA1 typically extends laterally for significant distances, sometimes kilometres. Periodically, sandy units contain basal gravel lags. Sandy FA1 units are characterized by sandstone to granular sandstone units that exhibit normal grading. Within FA1, sandy units preserving diverse architectural elements are recognized (sensu Miall, 2014), including channel-associated elements: channel elements (CH), scour hollows (SH) and lateral accretion (LA) (Fig. 4). Channel elements range in thickness from 0.4 to 2.0 m and extend laterally for 10.0 to 40.0 m (sheets can laterally extend for several kilometres) to laterally discontinuous multilateral trough-bedded sandstones (Fig. 4).

Facies Association 1 is interpreted to be parautochthonous (near-source) clastics and coarse sediment accumulations within a proximal

<sup>© 2024</sup> The Author(s). *Sedimentology* published by John Wiley & Sons Ltd on behalf of International Association of Sedimentologists, *Sedimentology* 

ĔΙ

across the Short Canyon and Mussentuchit members: modified from Miall (2010) Facies associations identified in outcron

3	or a acres associ	table of a decise associations facilities in caterop across the ones can you and reason according incomined from them (2010).	yon and masseman	it members, mo	ainea nom ivia	. (2010):	
FA	FA Sediment scale Facies codes	Facies codes	Architectural elements	Bounding surfaces	Bioturbation Stratigraphic intensity distribution	Stratigraphic distribution	Interpretation
FA	FA1 Boulder/cobble/ granule/sand	Gcb, GSe, Gmx, Gmm, Gst, Gsp, St, Si, Sm, Ss, Sh, GSe, Gst, Gsp, Gmm, Gmx	Crude bedding GB, CH, SH, LA	Third to seventh- order	0	Short Canyon Fluvial Member distribu fan	Fluvial distributive fan
FA	FA2 Sand/pebble/silt Sm, Gmx, St, Sp	Sm, Gmx, St, Sp	Massive	Fifth-order	0	Middle Mussentuchit	Sandy debris flow

Table 4. Unweathered and weathered colour index.

Colour	Colour Code
Light grey	G1 7/N
Medium grey	G1 6/N
Dark grey	G1 4/N
Light black	10R 6/3
Black	10R 4/3
Greyish yellow	5Y 8/4
Light brown	7.5YR 6/3
Light orange	10YR 8/2
White	N9

distributive fluvial fan (Benvenuti & Martini, 2002; Neves et al., 2005; Nichols & Fisher, 2007; Reading, 2009; Sambrook Smith et al., 2010; Weissmann et al., 2010; Fielding et al., 2012; Burnham & Hodgetts, 2018; Li et al., 2020). Despite some units exhibiting crude bedding, clasts are typically subangular to rounded, indicative of transport. even over a short distance. Due to the stacked nature of clastic-rich units and the multi-channel networks, the authors interpret that channel braiding and lateral movement (meandering) commonly reworked sediments and many internal structures (bars) were temporary. Crudely-bedded or sheetlike beds are interpreted to represent outwash linked to higher-energy pulses associated with tectonism and sediment unloading to the west. Subsequent hydraulic reworking occurred via a complex, high-energy, bed-load-rich, distal braid belt (Chen et al., 2017; Gao et al., 2020; Li et al., 2020; Zhang et al., 2021).

3653091, 0, Downloaded from https://onlinelibrary.wiley.com/doi/10.1111/sed.13211 by Stellenboseh University, Wiley Online Library on [04/07/2024]. See the Terms and Conditions (https://onlinelibrary.wiley.com/terms-and-conditions) on Wiley Online Library for rules of use; OA articles are governed by the applicable Creative Commons License

# Facies Association 2 (FA2)

Facies Association 2 (FA2), the last chance sand-stone, is limited to the middle Mussentuchit Member and is identified as an elongated sand-rich body composed of Sm, St, Sp and minor Gmx. In outcrops, FA2 reflects a light grey and is weathered to a light grey to greyish yellow (Fig. 7; Table 3). FA2 contains a sand-silt matrix with infrequent clay fractions and moderate to poor sorting. FA2 exhibits fifth-order erosive lower-bounding surfaces and fourth-order upper-bounding surfaces and fourth-order upper-bounding surfaces. This bedded unit typically is between 0.75 to 1.0 m thick, and these beds occur at the same stratigraphic interval for 20 to 30 km laterally. FA2 predominantly comprises coarse to fine sands that exhibit normal grading with infrequent pebbles,

Table 5. Interpreted bounding surfaces based on and modified from Vail et al. (1977) and Miall (2010).

Group	Timescale	Example	Sedimentation rate	Example	Rank
1	$10^{-6}$	Burst-varve	_	Lamina	0 <sup>th</sup>
2	$10^{-5}$ to $^{-4}$	Bedform migration	$10^5$	Ripple	1 <sup>st</sup>
3	$10^{-3}$	Bedform migration	$10^{5}$	Season dune increment	1 <sup>st</sup>
4	$10^{-2\ to\ -1}$	Bedform migration	$10^{4}$	Dune	$2^{\mathrm{nd}}$
5	100-10 <sup>1</sup>	Seasonal event (10-year flood)	$10^{2-3}$	Macroform growth	$3^{\mathrm{rd}}$
6	$10^{2-3}$	100-year flood	$10^{2-3}$	Macroform(splay, levée, immature palaeosol)	$4^{\rm th}$
7	10 <sup>3-4</sup>	Long-term process	$10^{0-1}$	Macroform(channel, palaeosol)	5 <sup>th</sup>

granules and clay rip-up clasts. Texturally, FA2 is typically massive, although, in the northern and southern mapping areas (Fig. 7), it exhibits sedimentary structures such as trough cross-bedding and planar cross-stratification. The widely distributed multi-taxic fossil material in the unit includes fragmentary vertebrate remains, high-density vertebrate microfossil bonebeds, and partial eggs and eggshell hash.

Facies Association 2 is interpreted as reflecting a large-scale, terrestrial, hyper-concentrated flow past the intersection point and distal to the alluvial fan (Benvenuti & Martini, 2002). FA2 would have been a large-scale sandy debris flow or sand sheet extending outward and covering the depocentre (Barkat et al., 2020; Li et al., 2020; Gardner & Dorsey, 2021; Yu et al., 2022). Of note, FA2's entombed fossil material reflects an accumulation of reworked multi-taxic, para-autochthonous fossil concentration (high of eggshell), emplaced within a singular flow likely related to decreased hydrodynamic energy related to lower slope or inertia energies.

# Stratigraphy

The Short Canyon Member was historically recognized as a southward thinning wedge, from the type section near the geographical location of the Short Canyon and terminating near I-70. The above observations expand the unit by ca 30 km (Figs 1 and 2). Secondly, historical observations have identified a persistent pebble lag between the Ruby Ranch and Mussentuchit members, as previously identified in the Mussentuchit Wash mapping area (Kirkland et al., 2016, and references therein). This was corroborated by Tucker

et al. (2022), who noted the persistent pebble lag between the Ruby Ranch and Mussentuchit members in the Mussentuchit Wash quadrangle; yet, with further exploration, this study identified a southward thickening lag to bedded conglomerate within the Willow Springs quadrangle (Figs 5C, 5F and 8) (Doelling et al., 2009). Observed thinning of the alluvial lenses in a west to east orientation trending to the foredeep, along with variable thickness laterally south to north, is interpreted to represent lateral stacking of multiple alluvial fans running parallel to the adjacent fold-and-thrust belt source. Thus, with supporting descriptions from Hunt et al. (2011), Doelling & Kuehne (2013) and Kirkland et al. (2016; and references therein), this study interprets the pebble lag to be the very distal exposure of the Short Canvon Member, which is variably exposed but laterally continuous for ca 50 km (Fig. 9). The observations herein are in agreement with those of Kirkland et al. (2016; and references therein) that the Short Canyon Member is bounded by disconformable contacts with the underlying Ruby Ranch Member and overlying Mussentuchit Member. The underlying contact is interpreted to have been erosive (downcutting into the Ruby Ranch Member), consistent with the interpretation of Doelling & Kuehne (2013). Within the present study area, the northerly wedge is 12.0 m thick, thinning to 5 cm pebble lag in the Mussentuchit Wash; however, this thickens to the south at a maximum of 80.0 cm observed just west of the Last Chance Desert. Based on this observation, the authors propose that the pebble lag between the Ruby Ranch and Mussentuchit members (observed in the Mussentuchit Wash and northern Willow Spring quadrangles) be defined

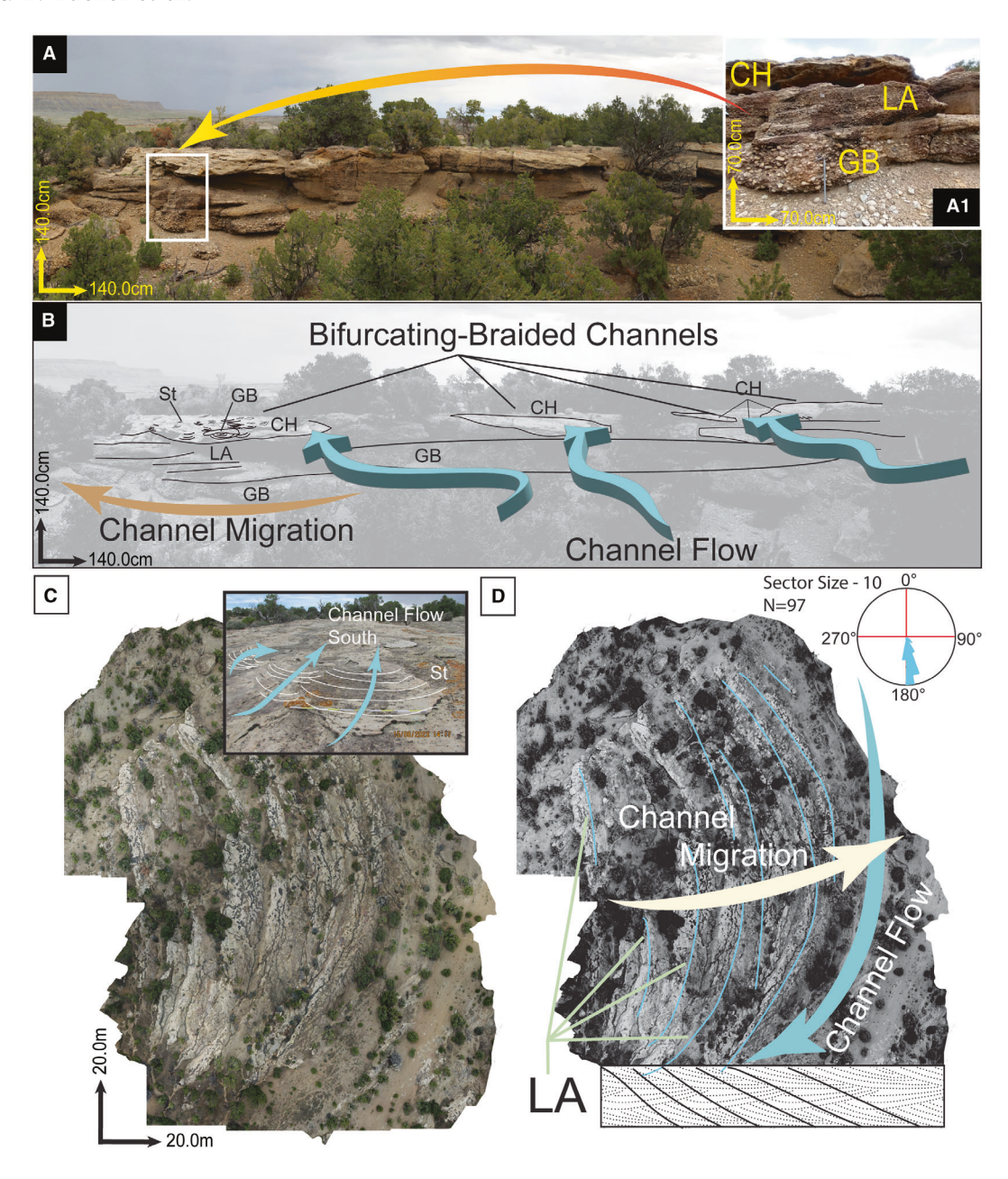


Fig. 4. (A) Photomosaic of FA1 near the type section at Short Canyon (north of the Moore Cutoff Road). (B) Interpretation of Photomosaic (A) with: GB – Gravel Bars; CH – Channels; LA – Lateral Accretion; St – Sandy Trough Cross-Stratification with the orientation of channel migration to the east and palaeoflow in a southerly orientation. (C) Photomosaic (aerial photograph) of FA1; (D) Interpretation of Photomosaic at a developed scroll bar with upper (St) Sandy Trough Cross-Stratification flowing south-east and channel migration to the east.

as a portion of the Short Canyon Conglomerate, thus expanding the total lateral extent of known Short Canyon Conglomerate strata to at least 50.0 km.

The 'middle' sandstone is a stratigraphically key marker horizon persistently exposed in the middle of the Mussentuchit Member (Figs 4A, 4C and 9). As mentioned above, this study

informally names this 'middle' sandstone the last chance sandstone and identifies it as a divisional unit between lower and upper Mussentuchit members. The designation of 'last chance sandstone' was selected based on the proximity to the Last Chance Desert in the southern portion of the mapping area (Fig. 1). Typically, the Mussentuchit Member is roughly

13633091, 0, Downloaded from https://onlinelibrary.wiley.com/doi/10.1111/sed.13211 by Stellenbosch University, Wiley Online Library on [04/07/2024]. See the Terms

and-conditions) on Wiley Online Library for rules of use; OA articles are governed by the applicable Creative Commons License

Fig. 5. (A) Typical disconformable contact of laterally extensive Short Canyon Member with underlying Ruby Ranch Member; (B) stacked succession of coarse trough cross-stratified sandstones and gravel bars; (C) unstratified or crudely bedded gravels; (D) pebble-rich coarse trough cross-stratified sandstones; (E) gravel lags with overlying Mussentuchit Member; and (F) and (F1) cobbles and boulders typical of the Short Canyon Member.

22 to 24 m thick, with the last chance sandstone occurring 11.0 to 12.0 m from the basal Short Canyon–Mussentuchit contact. However, the reader should note that the overall thickness of

the Mussentuchit Member ranges from 14.0 to 28.0 m, which affects the stratigraphic position of the last chance sandstone depending on location. Minor lithological variations occur within

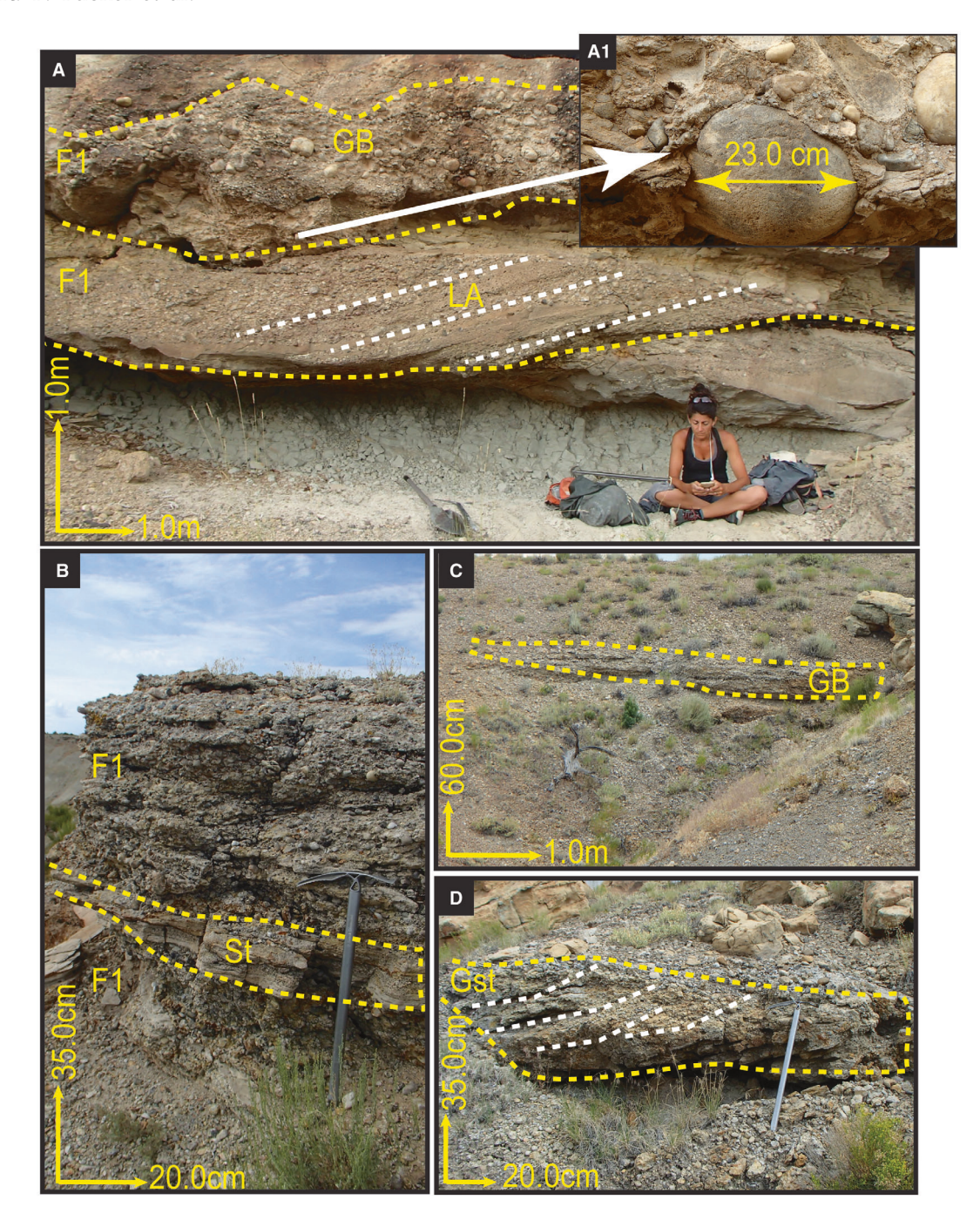


Fig. 6. (A) FA1 Concave-up channelization with co-occurring; LA – Lateral Accretion Form and GB – Gravel Bar with interbedded sandy FA1 lower-energy channelized flow and (A1) close-up of larger clastic material; (B) St – Minor trough cross-stratified interbedded between Gm – crudely-bedded conglomerates; (C) Exposed but poorly preserved lateral channel (GB) – Gravel Bar; (D) clastic-rich trough-set (Gst). Yellow dashed lines indicate higher-order bounding surfaces, and white dashed lines indicate internal geometries associated with lower-order bounding surfaces. Note to the reader: herein lithosomes are sedimentary structures observed in outcrop denoted by 'St', and facies 'F' are depocentres or palaeoenvironments.

this unit, either as a thick-bedded massive sandstone with normal internal grading (with or without a basal gravel lag), or as thinly-stacked trough sets and planar cross-stratified sets formed by hydraulic alteration. In either case, this consistent lithostratigraphic position of the

13653091, 0, Downloaded from https://onlinelibrary.wiley.com/doi/10.1111/sed.13211 by Stellenbosch University, Wiley Online Library on [04/07/2024]. See the Terms and Conditions (https://onlinelibrary.wiley.com/rerms-and-conditions) on Wiley Online Library for rules of use; OA articles are governed by the applicable Creative Commons License

Fig. 7. (A) Last chance sandstone in the Mussentuchit Wash quadrangle; (B) to (D) last chance sandstone in the Willow Springs quadrangle; (E) last chance sandstone in the Walker Flat quadrangle.

unit is defined as: (i) 0.5 to 1.0 m above Mussentuchit Ash Zone 1 (MAZ1); and (ii) 0.3 to 0.8 m below Mussentuchit Ash Zone 2 (MAZ2) (Tucker *et al.*, 2023).

# Geochemistry

To characterize and classify the four ash falls of Tucker *et al.* (2023), both XRD (Table 6) and XRF [Table 7 (majors) and Table 8 (minors)] analyses were utilized. Identification of the ash beds in the Mussentuchit Member follows Hong *et al.* (2019), with the ash beds consisting of 64 to 80% glass, 20 to 25% phenocrysts, and minor amorphous clays, which these units fulfil. Based on the XRD results, the presence of quartz crystals and more

significant amounts of plagioclase (10–20%) as opposed to orthoclase (0.8–4.5%), and XRF-based IUGS classification of volcanic rocks (Fig. 10), all four ash beds are classified as dacitic (Table 8).

According to the discrimination diagrams by Peccerillo & Taylor (1976) (Fig. 10A), these dacites are borderline tholeitic to medium-K calc-alkaline (Fig. 10B). Moderate levels of an unidentified amorphous fraction (39–53%) coupled with high  ${\rm SiO_2}$  values indicates that the amorphous fraction is predominantly volcanic glass, as opposed to meta-Kaolin. Although these observations broadly correspond with a lithology of crystal tuff, the age and levels of smectite present (13–20%) in these beds make tuffaceous bentonite a more appropriate lithological designation. Furthermore, field





Fig. 8. (A) Striking contrast between the underlying Short Canyon Conglomerate and overlying muds of the Mussentuchit Member. (B) Southward thickening wedge of the Short Canyon Member in the Cliffs of Insanity west of the Last Chance Desert (Willow Springs quadrangle).

observations include haystack erosional landforms, popcorn weathering, jigsaw puzzle clay fractures and nodular masses (so-called 'eggs'), in addition to the previous descriptions of significant amounts of Mg (mixing of brackish waters), mineral content (anhedral biotite and euhedral zircon), variation in internal layering, layer charge, variable clay ratios and colour modification when wet (Huff, 2016). All of these traits support their designation as K-bentonites. Overall, results suggest that MAZ1 to MAZ4 were deposited as primary dacitic ashfalls that experienced moderate devitrification and alteration to tuffaceous Kbentonites.

# Uranium-lead geochronology and stratigraphic age modelling

Ages of ash zones within the Mussentuchit Member have been previously constrained by high-precision CA-ID-TIMS U-Pb zircon geochronology and Bayesian age modelling, which Tucker

et al. (2023) used to establish probabilistic ages for fossil sites in the Mussentuchit Member stratigraphy. The current research expands on this previous work, but with a shifted focus onto establishing probabilistic ages, durations and deposition rates for lithostratigraphic units. Detrital zircon (within the 5% discordance cut-off) sample MC-07 was recovered from a medium to coarsegrained cross-bedded sandstone from the upper portion of the Short Canyon Member, ca 1.5 m below the local contact with the overlying Mussentuchit Member. Grains exhibit well-faceted euhedral crystal morphologies and clear detrital patterns such as rounding and abrasion, indicating a mixed-source assemblage of zircon grains (CL Images within File S2). One hundred and twentyseven detrital zircon grains analysed from sample MC-07 LA-ICP-MS dates ranging from 1765  $\pm$  45 to 94  $\pm$  3 Ma (Table S2). Ninety-two of those dates are between 115  $\pm$  6 Ma and 94  $\pm$  3 Ma. Six grains dated by CA-ID-TIMS yielded <sup>206</sup>Pb/<sup>238</sup>U dates from  $104.52 \pm 0.09$  to  $102.98 \pm 0.14$  Ma,

13653091, 0, Downloaded from https://onlinelibrary.wiley.com/doi/10.1111/sed.13211 by Stellenbosch University, Wiley Online Library on [04/07/2024]. See the Terms and Conditions (https://onlinelibrary.wiley.com/rerms-and-conditions) on Wiley Online Library for rules of use; OA articles are governed by the applicable Creative Commons License

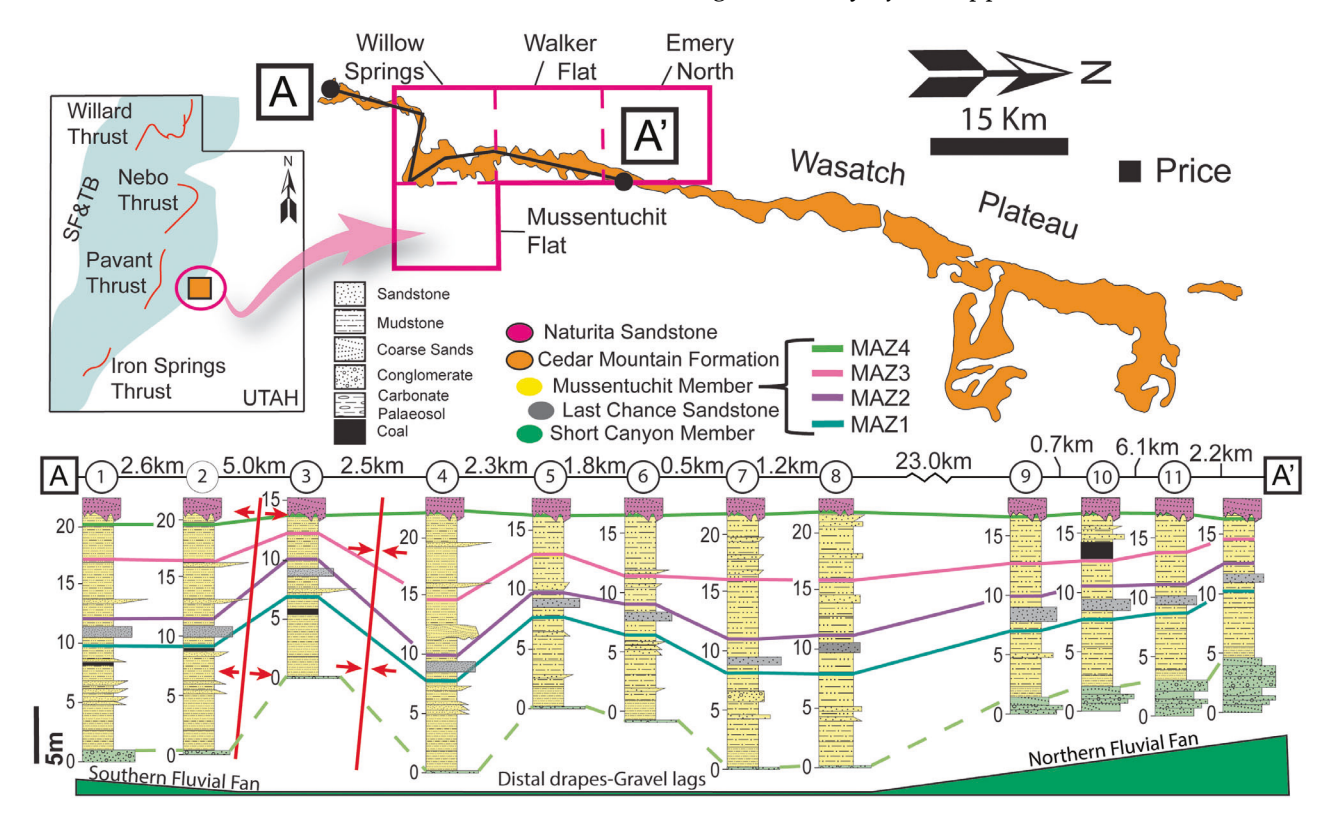


Fig. 9. Stratigraphic sections from South (left/A) to North (right/A') of the Short Canyon and Mussentuchit members with the Last Chance Desert Sandstone in grey (middle Mussentuchit). Modified from Tucker *et al.* (2023).

**Table 6.** Quantitative analysis by X-ray diffraction (XRD) analysis of four representative samples of the four ash layers (MAZ1–MAZ4) found within the Mussentuchit Member.

Ash layer	MAZ1	MAZ2	MAZ3	MAZ4
Sample	Burnt Leg	Ash Hole	Ash Hole	VAMP
Quartz	16.3	28.5	28.6	3.7
Kaolinite	0.6	0.4	0.5	5.3
Orthoclase	8.0	2.6	3.2	4.5
Plagioclase	20.5	10.4	10.6	13.3
Muscovite	8.8	0.4	0.4	0.4
Smectite	13.8	16.2	17.2	20.2
Amorphous	39.2	41.6	39.5	52.6

with the five youngest dates ranging from  $103.12 \pm 0.07$  to  $102.98 \pm 0.14$  Ma and overlapping at analytical uncertainties (Fig. 11; Table 9). A probabilistic maximum depositional age for the

MC-07 sandstone bed was established using the Bayesian algorithm of Keller et al. (2018), in similar fashion to Johnstone et al. (2019; for example, employing a uniform distribution prior), with likelihoods consisting of the five youngest zircon  $^{206}\text{Pb}/^{238}\text{U}$  dates. This method yields a 103.03  $\pm$ 0.096 Ma (2 sigma) maximum depositional age (MDA) for the sandstone bed represented by sample MC-07 (Fig. 12). This new MDA for the upper portion of the Short Canvon Member is consistent with posterior depositional ages for ash zones within the overlying Mussentuchit Member of 99.490 + 0.057/-0.050 Ma (MAZ1), 99.401 + (MAZ2), 0.058/v-0.066 Ma 99.191 + 0.057/-0.062 Ma(MAZ3) and 98.905 + 0.158/-0.183 Ma (MAZ4) established by Tucker et al. (2023), and statistically indistinguishable from the  $103.7 \pm 2.6$  Ma age for a tephra bed at the contact between the lowermost Buckhorn Conglomerate and the Ruby Ranch Member (Ludvigson et al., 2015).

To place quantitative constraints on the age of lithostratigraphic units within the Cedar Mountain Formation and establish a probabilistic depositional age for the Short Canyon Member,

Results of major element analysis via X-ray fluorescence (XRF) of fifteen volcanic ash samples collected from the four ash layers (MAZ1-MAZ4) collected from the Mussentuchit Member.

Ash layer MAZ1	MAZ1				MAZ2				MAZ3				MAZ4		
Sample	Ash Hole	Burnt Leg	Eureka	Eureka OMNH	Ash Hole	Burnt Leg	Eureka	OMNH	Ash Hole	Burnt Leg	Eureka	OMNH	Eureka	OMNH	VAMP
$\overline{\mathrm{Al}_2\mathrm{O}_3}$	19.82	17.02	19.80	15.47	19.88	20.62	16.17	21.89	15.72	15.23	21.04	20.33	15.24	17.61	21.17
CaO	0.76	1.12	0.77	0.25	0.81	0.65	0.37	0.69	0:30	0.43	0.37	0.74	0.19	0.36	0.71
$\mathrm{Fe_2O_3}$	2.66	3.25	2.78	3.46	2.95	3.70	3.74	3.19	3.84	3.85	2.92	3.73	3.11	4.14	2.87
$K_2O$	0.53	0.95	1.02	1.51	0.81	0.72	1.67	0.38	1.46	1.02	0.64	0.86	1.69	1.12	1.19
MgO	2.72	2.24	2.33	2.44	2.88	2.80	1.71	2.93	1.79	1.67	2.59	2.89	1.82	1.94	2.54
MnO	0.01	0.02	0.01	0.01	0.01	0.01	0.01	0.01	0.01	0.01	0.02	0.01	0.01	0.01	0.02
$Na_2O$	3.40	2.91	2.74	2.43	2.88	3.01	1.91	3.47	2.23	1.73	2.83	3.30	1.57	3.29	2.80
$P_2O_5$	0.05	0.03	0.07	0.01	0.03	0.05	0.02	0.04	0.01	0.02	90.0	0.05	0.04	0.03	0.09
$\mathrm{SiO}_2$	53.68	59.38	57.35	64.39	55.33	59.40	63.98	56.90	62.23	67.53	54.23	57.70	65.31	59.97	55.56
$TiO_2$	0.28	0.33	0.23	0.46	0.13	0.15	0.46	0.25	0.51	0.53	0.19	0.17	0.45	0.54	0.21
L.O.I.	16.47	13.62	13.04	10.09	14.88	9.92	10.86	10.91	12.83	8.85	15.33	10.96	11.01	11.45	13.63
TOTAL	100.38	100.87	100.15	100.52	100.58	101.03	100.91	100.67	100.92	100.86	100.23	100.75	100.44	100.45	100.79
			-	1	-			-	-						

Note that  $Cr_2O_3$  data for all the samples analysed is not included as amounts obtained were below the detection level.

1365991, 0, Downloaded from https://onlinelibrary.wiely.com/doi/10.1111/sed.13211 by Stellenbosch University, Wiley Online Library on [04/07/2024]. See the Terms and Conditions (https://onlinelibrary.wiley.com/terms-and-conditions) on Wiley Online Library for rules of use; OA articles are governed by the applicable Creative Commons License

13653091, 0, Downloaded from https://onlinelibrary.wiley.com/doi/10.1111/sed.13211 by Stellenbosch University, Wiley Online Library on [04/07/2024]. See the Terms and Conditions (https://onlinelibrary.wiley.com/terms/com/terms/see...)

and-conditions) on Wiley Online Library for rules of use; OA articles are governed by the applicable Creative Commons

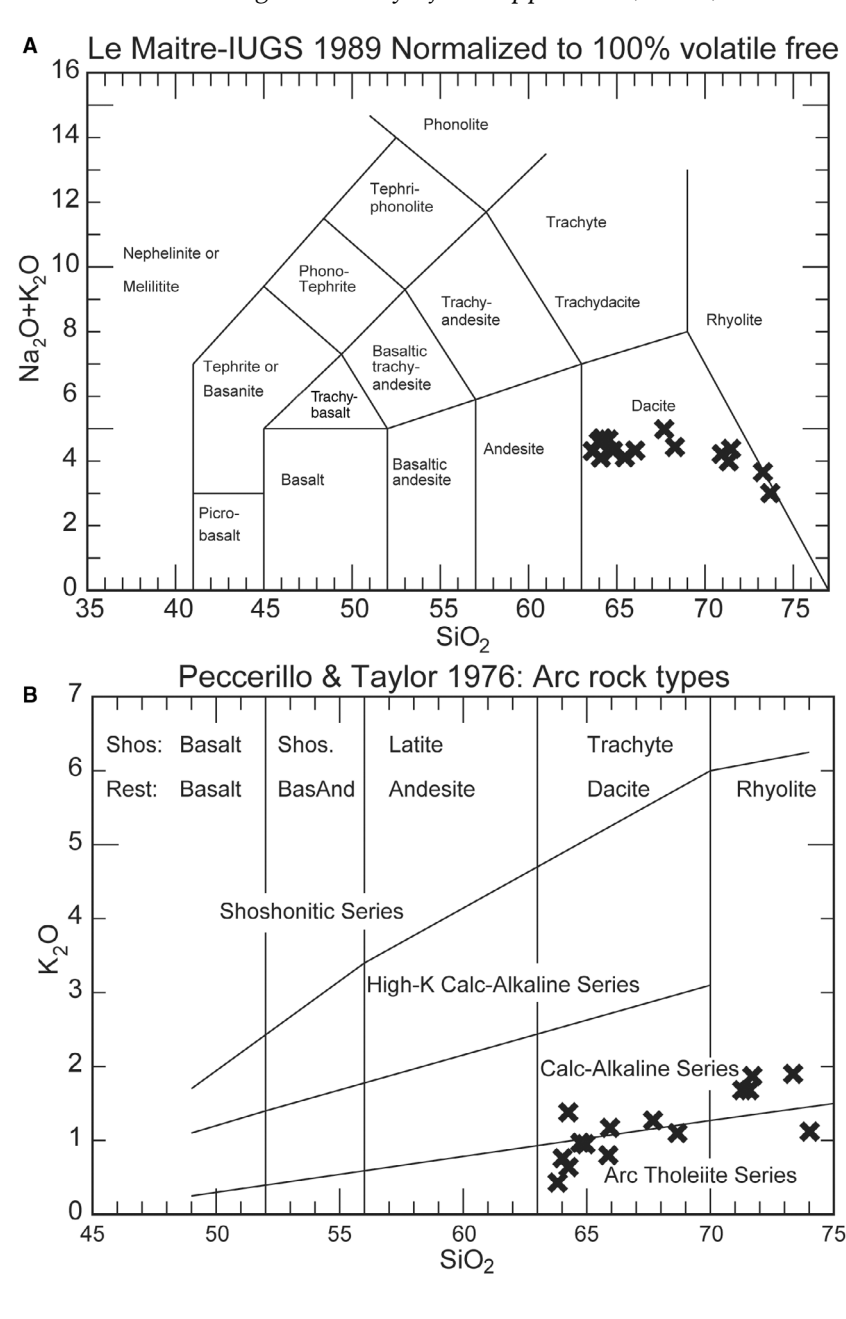


Fig. 10. Classification of volcaniclastics via: (A) La Maitre–IUGS; and (B) Peccerillo & Taylor (1976). Data within Tucker et al. (2023) or see File S2.

stratigraphic Bayesian age modelling was employed using the modified Bchron age model (Haslett & Parnell, 2008; Trayler et al., 2020) in the R programming language (R Core Team, 2022). Models were constructed using composite stratigraphic thicknesses for Cedar Mountain Formation strata with age likelihoods consisting of published depositional ages for Mussentuchit Member Ash Zones 1 to 4 (MAZ1–MAZ4) from Tucker et al. (2022), a tephra bed below the Ruby Ranch Member dated by Ludvigson et al. (2015), and both with (Model 1) and without (Model 2) the detrital zircon MDA likelihood for sample MC-

07. Figure 12 compares the two modelling scenarios to illustrate the sensitivity of model outcomes to a conservative broad uniform age likelihood represented by the MDA [constructed from a uniform distribution between 103.03 Ma (MDA) to 99.47 Ma (MAZ1)] and Gaussian-shaped tails equivalent to uncertainties on the MDA and MAZ1 age, respectively (e.g. Landing et al., 2021). Although both models may be considered equivalent within their 95% highest density intervals (HDI), the model incorporating the likelihood constructed from our new precise U–Pb zircon MDA for sample MC-07, (Model 1) prefers slightly older

R. T. Tucker et al.

20

Results of minor element analysis via laser ablation-inductively coupled-mass spectrometry (LA-ICP-MS) of fifteen volcanic ash samples col-

lected from the four ash layers (MAZ1-MAZ4) collected from the Mussentuchit Member

Table 8.

232.24 34.30 75.49 8.78 33.98 VAMP 73.00 36.43  $0.86 \\ 2.90$ 20.28 77.99 107.74 203.35 29.18 1.04 7.22 6.26 3.66 0.553.50 7.47 15.40 7.61 1.26 OMNH 76.79 30.60 53.75 01.34 115.87 282.48 1.536.5512.54 172.10 18.33 70.56 15.58 3.08 16.35 2.83 18.98 3.95 11.03 1.5010.04 15.65 9.97 19.60Eureka 98.35 218.19 64.53 22.32 93.93 73.65 38.97 213.53 19.56 1.04 23.66 85.43 16.98 2.49 12.561.65 8.12 1.4714.6 57.2 OMINH 13.46 26.32 189.78 1.131.97 142.04 52.32 11.73 43.67 0.896.03 2.91 0.4008.53 102.51 8.91 102.14Eureka 117.37 67.49 56.73 83.57 3.6648.03 83.79 17.44 62.89 11.29 1.559.85 1.76 5.0916.16 16.29  $1.22 \\ 9.36$ 137.08 9.0935.20 1.356.83 1.03 3.35 0.4858.55 91.37 36.42 38.64 273.91 79.01 Burnt Leg 10.16 122.98 2.88 0.58 0.503.38 0.80 24.50 29.35 87.83 73.29 25.36 230.55 18.39 1.13 17.76 32.87 20.61 75.70 14.17Hole Ash OMNH 9.26 14.19 52.68 64.151.0086.74 215.37 37.61 310.18 282.91 169.67 19.57 71.91 13.57 1.78 10.17 1.400.470.71 Eureka 112.19 106.24 6.25 4.88 16.16 95.93 19.95 0.7453.01 42.24 0.860.982.55 0.372.45 0.3511.97 8.01 28.9 55 27.16 42.52 88.38 37.84 6.95 $6.02 \\ 1.09$ 2.99 0.392.43 0.3543.04 10.25 8.05 0.77 1.01 54.90 33.11 72.87 204.90 Burnt Leg 33.19 55.46 47.10 14.02 13.65 96.10 20.49 9.560.926.620.930.980.43MAZ230.69 25.71 229.65 32.94 1.4813.51 239.21 Hole Ash OMNH 12.00 61.9850.08 24.04 2.223.17 18.00 12.65 0.3513.32 66.86206.88 28.11 11.73 10.75 3.64 48.81 Eureka 61.4933.04 213.08 50.02 103.76 43.39 2.6966.13 40.93 31.12 213.76 12.13 9.04 0.45 17.19 82.26 68.1864.29 21.69 65.19 0.97 3.65 37.82 76.23 31.98 1.155.5636.86 10.66 16.41 8.74 5.93 2.220.322.08 28.42 397.31 0.3116.71 Burnt Leg 32.153.48 3.56 8.6512.82 24.18 23.9920.75 67.75 16.18 2.51 1.66343.95 46.09 86.78 5.28 0.932.07 0.3 206.87 55.08 MAZ1 9.7 Ash Hole Ash layer Sample Zr Nb Mo Cs Cs Ce Ce Ce Ce Th Tb Ho Ho Zn Rb Sr Y ï ü

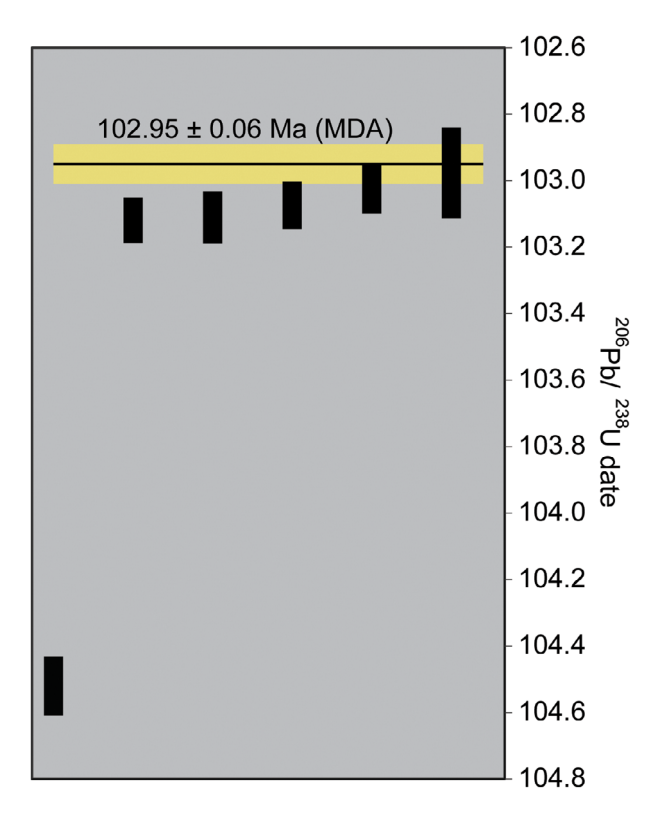


Fig. 11. Chemical abrasion – isotope dilution – thermal ionization mass spectrometry (CA-ID-TIMS)  $^{206}\text{Pb}/^{238}\text{U}$  zircon dates ( $\pm$  2 $\sigma$  uncertainties: black bars) for sandstone sample MC-07 from the Short Canyon Member. The Maximum Depositional Age (MDA) for the sandstone was established using all six detrital zircon dates input into the Bayesian algorithm of Keller *et al.* (2018).

accumulation paths through the Ruby Ranch Member and Short Canvon Member, leading to a wider range of accumulation paths compared to Model 2 results that exclude the MDA (Fig. 12A and B). Posterior ages generated in Model 1 and Model 2 for positions of interest are listed in Fig. 12C. Most noteworthy is that posterior ages for the Short Canyon Member conditioned by superposition, age likelihoods throughout the Cedar Mountain Formation, and representative long-term accumulation rates in both models suggest deposition of the Short Canyon Member likely occurred ca 2 to 3 Ma after the 103.03  $\pm$  0.096 Ma MDA produced by detrital zircon from sample MC-07. Model 1 predicts a 100.79 + 1.76/ -0.84 Ma age for the base and 100.15 + 1.47-0.53 Ma age for the top of the Short Canyon Member; whereas, Model 2 predicts a 100.44 + 1.35/-0.72 Ma age for the base and 100.08 + 1.14/-0.47 Ma age for the top of the Short Canyon Member. A ca 100 Ma age for deposition of the Short Canyon Member is generally consistent with geological evidence suggesting that the source of the Short Canvon Member conglomerate was fluvial fans developed from the Sevier highlands during renewed thrusting across south-central to north-central Utah (Hunt et al., 2011; Doelling & Kuehne, 2013; Kirkland et al., 2016; and references therein). It is important to consider that age determinations for the Short Canvon Member from our modelling could be biased if disconformable contacts between the Ruby Ranch Member and Short Canvon Member, as well as the Short Canyon Member and the Mussentuchit Member, represent long-lived hiatuses. However, the conservative credible intervals associated with these ages that are reflected by probabilistic accumulation scenarios likely encompass this geological

Also established from these age modelling results are long-term accumulation rates calculated from 95% HDI of model posterior distributions and thicknesses of stratigraphic intervals (Fig. 12C). In general, there are insignificant differences between accumulation rates generated from Model 1 (with MDA) versus those generated in Model 2 (without MDA), this study's focus is instead on the steepening of accumulation paths that is apparent in the lower to middle Mussentuchit Member portion of both age models (Fig. 12). The highest apparent long-term accumulation rates are represented in the last chance sandstone (transition from the lower to middle Mussentuchit Member), reaching a maximum of 42.8 + 72.9/ -20.8 m/Myr between MAZ1 and MAZ2. This signal of accelerated deposition transitioning from the lower to middle Mussentuchit Member (last chance sandstone) is interpreted to reflect the sediment-rich gravity flow (FA2) mentioned above (Trayler et al., 2020). After that, relaxation to 29.0 + 19.1/-7.9 m/Myr between MAZ2 MAZ3, and a return to rates of ca 10 to 20 m/Myr above MAZ3, also characteristic of earlier Ruby Ranch Member deposition (Fig. 12C). If the disconformity between the Short Canvon and Mussentuchit members represents a protracted hiatus, this rapid deposition may have also been characteristic of lower Mussentuchit Member deposition; however, the current construction of our Cedar Mountain Formation age model cannot predict the hiatus durations for Ruby Ranch Member-Short Canvon Member and Short Canvon Member-Mussentuchit Member disconformable contacts. Future work establishing high-precision detrital zircon MDA constraints in the Ruby Ranch Member could help to better estimate hiatus durations

In the sample column, z1, z2, etc. are labels for analyses composed of single zircon grains that were annealed and chemically abraded (Mattinson, 2005) Table 9.

										Radiog	Radiogenic isotope ratios	ratios					
Sample (a)	LA-ICPMS spot label	Th (b)	$^{206}\text{Pb*} \times 10^{-13}$ (c)	$^{206}{ m Pb*} \times 10^{-13} { m mol}$ (c)	mol % <sup>206</sup> pb* (c)	Pb* (pg) (c)	${ m Pb_c} \ { m (pg)} \ { m (c)}$	Pb* Pb <sub>c</sub> (c)	<sup>206</sup> Pb <sup>204</sup> Pb (d)	<sup>208</sup> Pb <sup>206</sup> Pb (e)	<sup>207</sup> Pb <sup>206</sup> Pb (e)	% err (f)	<sup>207</sup> Pb <sup>235</sup> U (e)	% err (f)	<sup>206</sup> Pb <sup>238</sup> U (e)	% err (f)	Corr.
MC-07	158	0.342	0.2260	0	98.06%	5.4	0.37	15	929	0.109	0.048200	0.493	0.108581	0.545	0.016346	0.085	0.659
9z	193	0.374	0.5676	9.	99.57%	13.7	0.20	29	4177	0.120	0.048207	0.127	0.107133	0.177	0.016125	0.067	0.839
z3	131	0.460	0.2152	2	99.28%	5.3	0.13	41	2507	0.147	0.048149	0.234	0.106994	0.278	0.016124	0.077	0.672
z2	157	0.472	0.3715	22	99.42%	9.2	0.18	51	3125	0.151	0.048096	0.169	0.106837	0.216	0.016118	0.070	0.763
$z_1$	190	0.383	0.4314	4	99.59%	10.4	0.15	71	4395	0.123	0.048230	0.174	0.107084	0.214	0.016110	0.071	0.678
z4	116	0.363	0.0596	9.	96.65%	1.4	0.17	∞	539	0.116	0.048349	0.953	0.107298	1.029	0.016103	0.134	0.617
	Isotopic dates	ates															
Sample (a)	<sup>207</sup> Pb <sup>206</sup> Pb ± (g)	207 ± 235 (f) (g)	<sup>207</sup> Pb <sup>235</sup> U (g)	± (f)	<sup>206</sup> Pb <sup>238</sup> U :	# (f) 1	Include in weighted mean?	in weig	ghted m		Weighted mean calculations (95% confidence interval)	ean calcr	ılations erval)				
MC-07																	
z2	108.01	11.64 10	104.67	0.54 1	104.52	0.09				7.7	206Pb/238 U $\pm$ random (+tracer) [+decay constant]	$J \pm \text{rand}$	om (+tracer)	(+deca	y constant]	MSWD = 1.6	0 = 1.6
9z	108.40 2	2.99 10	103.34	0.17 1	103.12	0.07	×			11	$\pm$ 0.05 (0.06) [0.12]	[0.12]				pof = 0.17	0.17
z3	105.55 5	5.52 10	103.21	0.27 1	103.11 (	0.08	×									n=5	
z2	102.92 4	4.00 10	103.07	0.21 1	103.07	0.07	×										
z1	109.50 4	4.10 10	103.29	0.21 1	103.03	0.07	×										
z4	115.33 2	22.47 10	103.49	1.01	102.98	0.14	×										
The mod	The medel Th. II metic and coloniated from the medicannic 208 Dh. 206	00 00111	0010100	ft mont	1:000	208		1	ond the	207ph /23	5rr dete mb	Au Lub	i Com omo		J. C. C. C. D.		1,1,1,1,1

% <sup>206</sup>Pb\* is with respect to radiogenic and blank Pb. The measured ratio was corrected for spike and fractionation only. Pb fractionation correction is Corrected for fractionation and spike. Common Pb in zircon analyses is assigned to procedural blank with the composition of  $^{206}\text{Pb}/^{204}\text{Pb} = 18.04 \pm 0.61\%$ ;  $^{207}\text{Pb}/^{204}\text{Pb} = 15.54 \pm 0.52\%$ ;  $^{208}\text{Pb}/^{204}\text{Pb} = 37.69 \pm 0.63\%$  (1 sigma).  $^{206}\text{Pb}/^{238}\text{U}$  and  $^{207}\text{Pb}/^{206}\text{Pb}$  ratios corrected for initial disequilibrium in  $^{230}\text{Th}/^{238}\text{U}$  using a D (Th-U) of 0.20  $\pm$  0.05 (1 sigma). Errors are 2 sigma, propagated using algorithms of Schmitz & Schoene (2007) and Crowley *et al.* (2007). Calculations based on the decay constants of Jaffey *et al.* (1971). <sup>206</sup>Pb/<sup>238</sup>U and <sup>207</sup>Pb/<sup>206</sup>Pb dates corrected for initial disequilibrium in <sup>230</sup>Th/<sup>238</sup>U using a D (Th-U) of 0.20  $\pm$  0.05 0.18  $\pm$  0.03 (1 sigma) %/amu (atomic mass unit) for single-collector Daly analyses, based on recent EARTHTIME 202 Pb-#Pb ET2535 tracer solution analyses. The model Th-U ratio was calculated from the radiogenic <sup>208</sup> Pb/<sup>206</sup>Pb ratio and the <sup>207</sup>Pb/<sup>235</sup>U date. Pb\* and Pbc are radiogenic and common Pb, respectively. mol

13653091, 0, Downloaded from https://onlinelibrary.wiley.com/doi/10.1111/sed.13211 by Stellenbosch University, Wiley Online Library on [04/07/2024]. See the Terms and Conditions (https://onlinelibrary.wiley.com/terms-and-conditions) on Wiley Online Library for rules of use; OA articles are governed by the applicable Creative Commons. Licensea

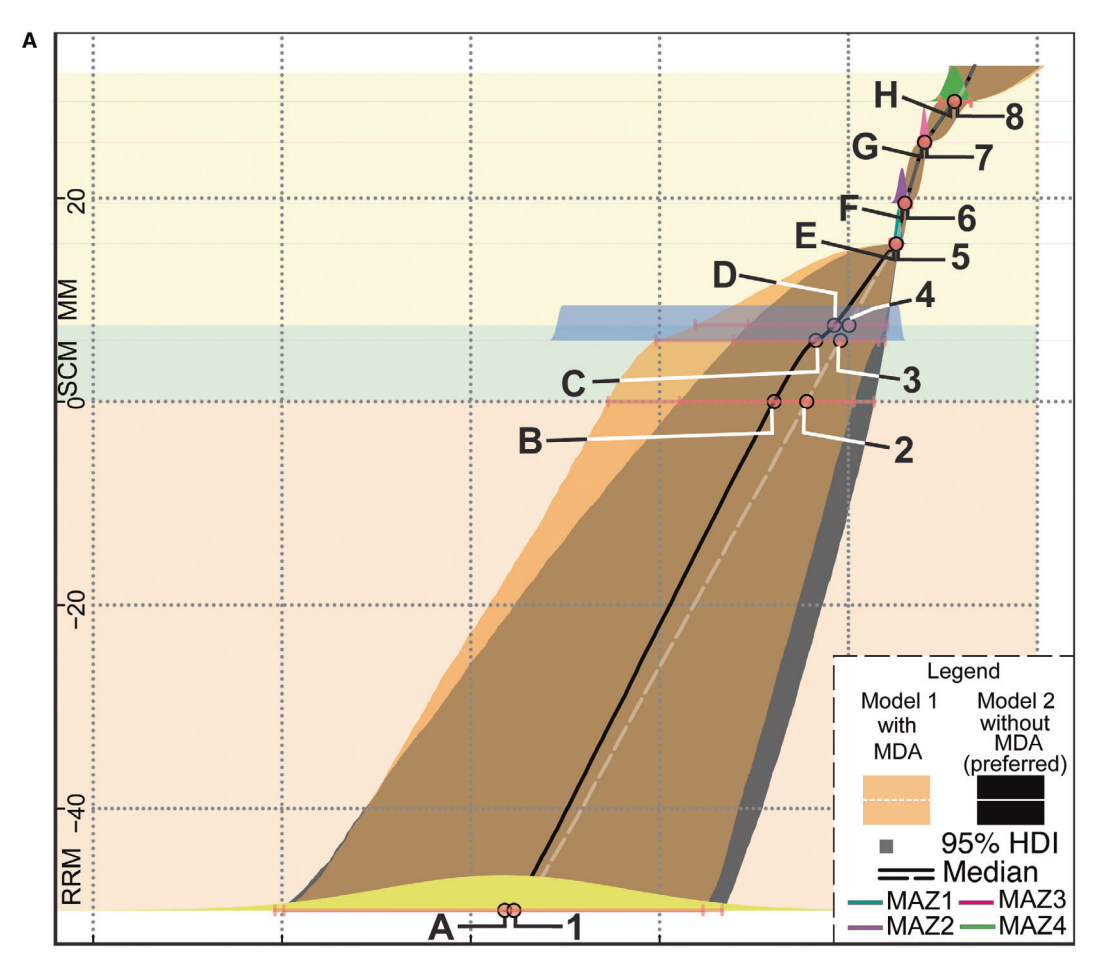


Fig. 12. (A) Bayesian age-stratigraphic models through the Short Canyon and Mussentuchit members constructed with the modified Bchron age model of Trayler et al. (2020). Models were constructed using U-Pb zircon CA-ID-TIMS (chemical abrasion-isotope dilution-thermal ionization mass spectrometry) ages of ash zones in the Mussentuchit Member presented in Tucker et al. (2023), the age of a tephra bed underlying the Ruby Ranch Member presented in Ludvigson et al. (2015) and with our new Maximum Depositional Age (MDA) for sample MC-07 in the Short Canyon Member represented by the broad orange likelihood distribution. Also shown are modelling results without incorporating the MDA for sample MC-07. While the 95% highest density intervals (HDI) of both models overlap, incorporating the Short Canyon Member MDA as a likelihood (median black line with orange field HDI) produces a wider range in the 95% highest density interval (HDI) and a slightly older most likely accumulation path. The authors consider the model incorporating the Short Canyon Member MDA more suitable for estimating the timing of deposition and accumulation rates due to the unknown duration of disconformities that bound the Short Canyon Member. Note: 'A' to 'H' correspond to incorporating MDA, '1' to '8' lacks MDA; background colour: Ruby Ranch Member (RRM) - peach; Short Canyon Member (SCM) - light green; and Mussentuchit Member (MM) - light yellow. (B) (B1) Long-term sediment accumulation rates calculated from posterior distributions established in Bayesian age-stratigraphic models (A) through the Ruby Ranch, Short Canyon and Mussentuchit members, and composite stratigraphic thicknesses. Black-dashed arrows indicate decreased rates; whereas, the pink arrow indicates increased rates. (B2) The shift in accumulation rates in the lower to middle Mussentuchit Member is interpreted to reflect the interpreted sediment gravity flow across the depositional zone, herein recognized as the last chance sandstone. (C) Tables of results of Bayesian stratigraphic age modelling for models constructed with ('A' to 'H') and without ('1' to '8') the new detrital zircon MDA for the SCM (C1). Posterior ages represent the median and 95% credible intervals of model paths for stratigraphic positions of interest. (C2) Long-term accumulation rates were calculated from the posterior distributions at the top and bottom of stratigraphic intervals and their respective composite thicknesses. (C3) Duration of the SCM calculated from the difference between posterior distributions for the base and top of the SCM stratigraphic interval. All uncertainties listed are derived from 95% credible intervals of the model data.

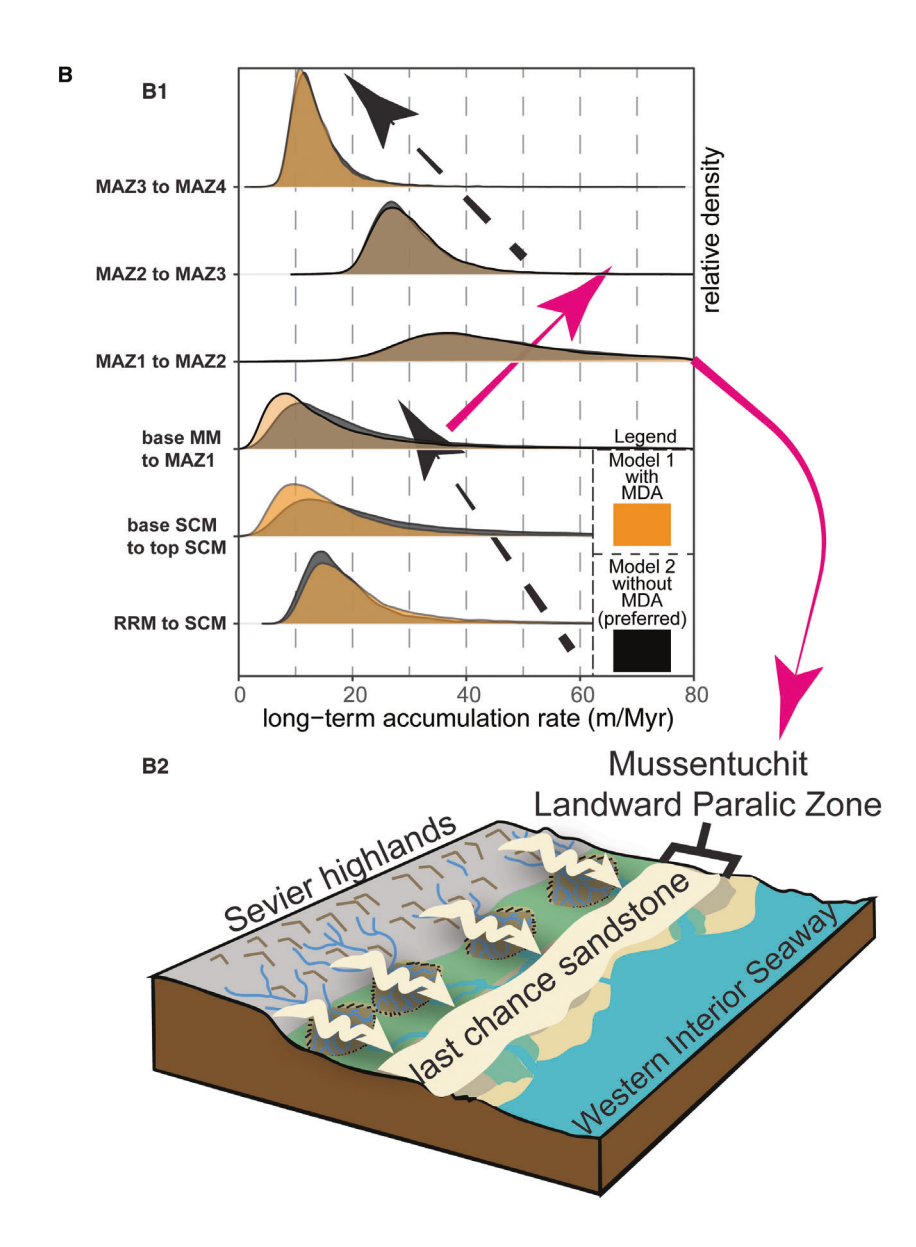


Fig. 12. Continued

between members of the Cedar Mountain Formation and characteristic long-term accumulation rates for these units.

# **DISCUSSION**

This study provides: (i) a detailed facies description of the Short Canyon Member and last chance sandstone coupled with revised depositional history; (ii) inferences about the local to regional tectonically linked sedimentary history; (iii) confirmed historical linkages or suggested new correlations to key units in the westerly adjacent fold-and-thrust belts along with regional transgression and regression cycles found elsewhere in the

Western Interior Seaway; and (iv) new stratigraphic linkages across the Western Interior.

Clastic strata of the Short Canyon Member were described as three separate conglomerate beds alongside co-occurring sands and carbonaceous shales with limited exposure north of I-70 (western San Rafael Swell) (Doelling & Kuehne, 2013; Kirkland *et al.*, 2016). This study expands the known exposure of the Short Canyon Member to the Last Chance Desert south of I-70. North of I-70, the observations noted here concur with the conclusion of Doelling & Kuehne (2013) and Kirkland *et al.* (2016) that the Short Canyon Member forms a northward thickening stratigraphic interval. Herein, it is proposed that the gravel lag observed in the quadrangles of Willow Springs and

13653091, 0, Downloaded from https://onlinelibrary.wiley.com/dov/10.1111/sed.13211 by Stellenbossch University, Wiley Online Library on [0407/2024]. See the Terms and Conditions (https://onlinelibrary.wiley.com/terms-and-conditions) on Wiley Online Library on [0407/2024]. See the Terms and Conditions (https://onlinelibrary.wiley.com/terms-and-conditions) on Wiley Online Library on [0407/2024]. See the Terms and Conditions (https://onlinelibrary.wiley.com/terms-and-conditions) on Wiley Online Library on [0407/2024]. See the Terms and Conditions (https://onlinelibrary.wiley.com/terms-and-conditions) on Wiley Online Library on [0407/2024]. See the Terms and Conditions (https://onlinelibrary.wiley.com/terms-and-conditions) on Wiley Online Library on [0407/2024]. See the Terms and Conditions (https://onlinelibrary.wiley.com/terms-and-conditions) on Wiley Online Library on [0407/2024]. See the Terms and Conditions (https://onlinelibrary.wiley.com/terms-and-conditions) on Wiley Online Library on [0407/2024]. See the Terms and Conditions (https://onlinelibrary.wiley.com/terms-and-conditions) on Wiley Online Library on [0407/2024]. See the Terms and Conditions (https://onlinelibrary.wiley.com/terms-and-conditions) on Wiley Online Library on [0407/2024]. See the Terms and Conditions (https://onlinelibrary.wiley.com/terms-and-conditions) on Wiley Online Library on [0407/2024]. See the Terms and Conditions (https://onlinelibrary.wiley.com/terms-and-conditions) on Wiley Online Library on [0407/2024]. See the Terms and Conditions (https://onlinelibrary.wiley.com/terms-and-conditions) on Wiley Online Library on [0407/2024]. See the Terms and Conditions (https://onlinelibrary.wiley.com/terms-and-conditions) on Wiley Online Library on [0407/2024]. See the Terms and Conditions (https://onlinelibrary.wiley.com/terms-and-conditions) on Wiley Online Library on [0407/2024]. See the Terms and Conditions (https://onlinelibrary.wiley.com/terms-and-conditions) on Wiley Online Library on [0407/2024]. See the Terms and Conditions (https:/

**C1** 

C2

N	lode	el '	with	MDA	<b>1</b> , r	osteri	or	ages	

Fig. 12 A	Positions	0.025	0.5	0.975	ids	age (Ma)	+	-
Н	29.5	98.697	98.875	99.030	MAZ4	98.875	0.154	0.178
G	25.5	99.136	99.194	99.248	MAZ3	99.194	0.054	0.058
F	19.5	99.333	99.402	99.455	MAZ2	99.402	0.052	0.069
Е	15.5	99.448	99.495	99.560	MAZ1	99.495	0.066	0.047
D	7.5	99.622	100.151	101.623	SCMtop	100.151	1.472	0.529
С	6	99.679	100.345	102.036	MC-07	100.345	1.692	0.665
В	0	99.943	100.787	102.545	SCMbase	100.787	1.759	0.844
A	-50	101.540	103.640	105.979	RRMbase	103.640	2.339	2.100

Model without MDA, posterior ages

Fig. 12 A	Positions	0.025	0.5	0.975	ids	age (Ma)	+	-
8	29.5	98.707	98.878	99.038	MAZ4	98.878	0.160	0.171
7	25.5	99.135	99.193	99.246	MAZ3	99.193	0.054	0.058
6	19.5	99.337	99.402	99.456	MAZ2	99.402	0.053	0.066
5	15.5	99.445	99.494	99.557	MAZ1	99.494	0.063	0.049
4	7.5	99.585	99.994	101.060	SCMtop	99.994	1.066	0.409
3	6	99.611	100.084	101.219	MC-07	100.084	1.135	0.473
2	0	99.725	100.442	101.789	SCMbase	100.442	1.348	0.717
1	-50	101.337	103.543	106.075	RRMbase	103.543	2.532	2.206

# CMF accumulation rates without and with MDA

1.7. 1.1	thickness	With MI	)A				
accumulation intervals	unckness	0.025	0.5	0.975	rate (m/Ma)	+	-
MAZ3-MAZ4	4	8.0	12.5	25.8	12.5	13.3	4.4
MAZ3-MAZ2	6	21.1	29.0	48.0	29.0	19.1	7.9
MAZ2-MAZ1	4	22.0	42.8	115.7	42.8	72.9	20.8
base MM to MAZ1	8	1.9	6.1	30.6	6.1	24.5	4.2
base SCM to top SCM	7.5	4.6	13.7	49.9	13.7	36.2	9.1
base RRM to base SCM	50	10.3	18.4	57.3	18.4	38.9	8.1

	accumulation intervals	thickness	Without MDA						
			0.025	0.5	0.975	rate (m/Ma)	+	-	
	MAZ3-MAZ4	4	8.2	12.7	27.1	12.7	14.4	4.5	
	MAZ3-MAZ2	6	21.0	28.6	46.8	28.6	18.2	7.5	
	MAZ2-MAZ1	4	22.9	43.8	117.3	43.8	73.5	21.0	
	base MM to MAZ1	8	2.6	8.0	40.8	8.0	32.8	5.4	
	base SCM to top SCM	7.5	6.2	19.7	111.2	19.7	91.5	13.5	
ſ	base RRM to base SCM	50	9.6	16.7	40.6	16.7	23.9	7.1	

\_\_\_\_\_\_

duration of SCM	2.50%	50%	97.50%	duration (Ma)	+	-
model without MDA	0.067	0.381	1.211	0.38	0.83	0.31
model with MDA	0.150	0.549	1.637	0.55	1.09	0.40

Fig. 12. Continued

C3

### 26 R. T. Tucker et al.

Mussentuchit Flat corresponds with the Short Canyon Member. Sedimentation within the Short Canvon Member is interpreted to reflect a distributive fluvial fan (FA1), with deposits affected by hydraulic reworking (Benvenuti & Martini, 2002; 2009). Based on Doelling Reading, Kuehne (2013) and Kirkland et al. (2016), along with in-field observations, the three-tiered conglomerates indicate successive clastic transport and emplacement in this area of the southward portion of an eastward flowing distributive fan linked to activity in the adjacent thrust belt. However, the interbedded channel sands indicate a more allochthonous sediment source and, therefore, could reflect a two-part sediment influx into the depocentre. Finer sediments, including grevblack carbonaceous mudrocks (shales) and evaporites, described by Doelling & Kuehne (2013), are interpreted to reflect deposition within a distal floodplain. This carbonaceous succession of muds may reflect sedimentation similar to that of the lowermost Mussentuchit Member, indicating stronger genetic linkages than previously thought (Tucker et al., 2020). In contrast, our newly named last chance sandstone of the middle Mussentuchit Member is interpreted to represent an amalgamated sandy gravity flow (FA2) that blanketed the whole of the landward paralic depositional area (Mussentuchit Member), likely composed of localized sediments and parautochthonous fossil material. In the north and south, these facies preserve hvdraulic evidence of reworking channelization.

In a comparative study to ground-truth sediment sources within these evolving depocentres, detrital zircon records first published by Tucker et al. (2020) and detrital zircon records from the Short Canyon Member (this study) were compared with that of the recent study by St. Pierre & Johnson (2022) in consideration of a possible central Utah linkage to a late Early Cretaceous, northeasterly flowing, 'California Style' river in a large basin-axial fluvial system (Fig. 13). This comparison stems from similarities of detrital zircon data presented by Tucker et al. (2020) and St. Pierre & Johnson (2022), along with variable palaeocurrent reconstructions similar and dissimilar to St. Pierre & Johnson (2022) for the Cedar Mountain Formation of central Utah (Garrison Jr. et al., 2007; Dickinson & Gehrels, 2008; Hunt et al., 2011; Suarez et al., 2012, 2014; Tucker et al., 2020). Therefore, detrital zircon grains from the Cedar Mountain Formation can be grouped into three distinct source terranes: (i) Cordilleran Arc (90-250 Ma); (ii) Orogen-transverse from the

Sevier fold-and-thrust belt (250-1200 Ma and 1900-3500 Ma); and (iii) Orogen-parallel from the Mogollon highlands (1200–1900 Ma). Overall, excluding the cosmopolitan detrital history of the lowermost Buckhorn Conglomerate Member, the Cedar Mountain Formation detrital zircon data present an ever-increasing input of Cordilleran Arc detritus. If the significant Mesozoic populations are excluded to constrain relationships between autochthonous to parautochthonous (Sevier fold-and-thrust belt clastics and sediments) and allochthonous sediments (Yavapai-Mazatzal and up-drainage sediments) or respectively orogen-transverse and orogen-parallel (axial), variable mixing of multiple sediment sources is observed.

In contrast to the model of St. Pierre & Johnson (2022), the present study found a more significant input from the westward-adjacent Sevierorogen-transverse source with moderate to minor orogen-parallel sources progressing up-section (Fig. 13). This is interpreted to reflect that fluvial input into the alluvial plain of the landward coastal margin of the western Cedar Mountain Formation consists largely of parautochthonous Sevier-sourced detritus (similar to Suarez et al., 2014). This could reflect factors such as the distance from southern sources and distal to the proposed 'Cretaceous Distributive Fluvial System' along with relatively close palaeogeographical proximity to the Sevier fold-and-thrust belt when compared to the Kaiparowits depocentre. This pattern is reflected in the last chance sandstone, interpreted to be a depocentre-wide, sandy debris (sheet) flow that displays a distinctly parautochthonous (Sevier fold-and-thrust belt) pattern. The authors postulate that the source of this sediment could have been a punctuated, singular mass debris flow during this intra-volcanic phase (stratigraphically situated between MAZ1 and MAZ2). In contrast to this observed pattern is the strikingly different sample recovered from the Short Canyon Member, containing the largest component of allochthonous sediments (extrabasinal), which is interpreted as a two-part sedimentation process. This study interprets a majority (not all) of lesser parautochthonous clastics (intra-basinal) and sediments to reflect recycledunroofed parautochthonous Sevier highland siliciclastics that have been mixed with a substantial influx of orogen-parallel detritus, coinciding coevally with the rejuvenated thrusting across Utah.

In comparison to previous studies, the authors initially noticed a slight dissimilarity between the

13653091, 0, Downloaded from https://onlinelibrary.wiley.com/doi/10.1111/sed.13211 by Stellenbosch University, Wiley Online Library on [04/07/2024]. See the Terms and Conditions (https://onlinelibrary.wiley.com/rerms-and-conditions) on Wiley Online Library for rules of use; OA articles are governed by the applicable Creative Commons License

Fig. 13. Comparison to St. Pierre & Johnson (2022) with detrital zircon data first presented in Tucker *et al.* (2020) for the Buckhorn Conglomerate, Ruby Ranch and Mussentuchit members, along with the Short Canyon from this study. Zircon populations are subdivided in accordance with St. Pierre & Johnson (2022) into: (i) Cordilleran Arc with dates younger than 250 Ma (*in grey*); (ii) Orogen-transverse (Sevier fold-and-thrust belt) with dates 250 Ma–1.2 Ga along with 1.9–3.5 Ga (*in orange*); and (iii) Orogen-parallel with dates 1.2 to 1.9 Ga (*in blue*). Palaeogeographical reconstruction of western North America and the Cretaceous distributive fluvial system are based on Dickinson & Gehrels (2008); Oboh-Ikuenobe *et al.* (2008); Suarez *et al.* (2012, 2014); St. Pierre & Johnson (2022); and figure modified from Tucker *et al.* (2022). *Note*: Greater circle plots display all grain populations (i) to (iii); smaller circle plots display only pre-250 Ma grain populations.

### 28 R. T. Tucker et al.

Short Canyon Member and the underlying Buchhorn Conglomerate, which would bolster observations made by Hunt et al. (2011) and Kirkland et al. (2016) concerning the dissimilarity between the two sedimentary successions (Fig. 13). The present datasets offer evidence that agrees with Hunt et al. (2011), who suggested that during the middle Cretaceous (Albian/Aptian - Cenomanian), the greater 'Cretaceous Distributive Fluvial System' was geographically east (Yellow Cat Member of the Cedar Mountain Formation) of the more westerly Buckhorn depocentre and had marginal influence on the easterly orogen-transverse systems. However, the siliciclastics of the Short Canyon Member run counter to this model, suggesting rather that during this short phase, the 'Cretaceous Distributive Fluvial System' possibly had a more significant influx of maturated sediments into this westerly depocentre, likely linked to heightened influx of sediment across the foredeep during the rejuvenated thrusting across southern and central Utah. Lastly, this sedimentological analysis shows evidence for much of the sedimentary detritus reflecting easterly flowing orogen-transverse distal fluvial systems transporting sediments through the landward paralic depocentres of the Mussentuchit Member with eventual deposition into the adjacent Western Interior Seaway (Tucker et al., 2022, 2023) in agreement with reconstructions by Suarez et al., 2014 (see fig. 5D in Suarez et al., 2014).

# Geochemistry

Contractional events in the adjacent Sevier foldand-thrust belt were contemporaneous with a voluminous volcanic flare-up in the westerly lying Cordilleran Arc associated with magmatism that produced the Sierra Nevada Batholith, Peninsular Ranges Batholith and the Atlanta Lobe of the Idaho Batholith (Chapman et al., 2021). Based on this study's broad-spectrum analysis via XRD and XRF, the analysed dacite (borderline tholeiitic to medium-K calc-alkaline) ashfalls cannot be ascribed to a unique source; however, based on the stratigraphic proximity between ashfalls, representing only 0.6 Ma (MAZ1-MAZ4), it is reasonable to infer that regional volcanic flare-ups were recurrent with the earliest phases of volcanic activity at ca 100 Ma ('Phase C') in the Sierra Nevada Batholith (DeCelles & Graham, 2015; Paterson & Ducea, 2015; Balgord et al., 2021; Schwartz et al., 2021) and ca 105 to ca 87 Ma in the Idaho Batholith (Gaschnig et al., 2011).

For this timeframe, around 100 Ma, recent interpretations by Hildebrand & Whalen (2021b) and Hildebrand et al. (2022) indicate a possible shift from a retro arc, foreland style foredeep to a collisional foredeep coeval to the Peninsular Ranges Orogen. Hildebrand et al. (2022) suggest that this shift occurred in an 11 Ma interval before the Cenomanian-Turonian. Based on the aforementioned reconstruction, this process may have been initiated during the Albian-Cenomanian transition. It could, therefore, be a mechanism for the transition from forebulge to foredeep sedimentation for the Short Canyon and Mussentuchit members in the western uppermost Cedar Mountain Formation (Currie, 1997, 2002; DeCelles et al., 2009; Lawton et al., 2010; Tucker et al., 2020, 2022; Balgord et al., 2021). When the discrimination diagrams modified from Hildebrand et al. (2022, and references therein), namely Nb/Y and Ta/Yb, are applied to the Mussentuchit Member ashfall deposits, the post-collision signatures obtained mirror those of Hildebrand & Whalen (2021a, 2021b) and Hildebrand et al. (2022), rather than the arc signatures that were expected (Fig. 14). Although this hypothesis requires further testing, the initial data suggest a meaningful linkage between the Peninsular Ranges arc and distal emplacement of ashfall in the collisional foredeep in central Utah; thus, one of the following can be substantiated: (i) the shift to a collisional foredeep occurs during the Albian-Cenomanian Transition, and the ashes of the Mussentuchit Member were deposited during the last phases of the retro-arc style foredeep; or (ii) the shift to a collisional foredeep marginally predated the earlier estimates as given by Hildebrand & Whalen (2021b) and Hildebrand et al. (2022), thereby occurring during the Albian-Cenomanian transition. The above results suggest that scenario two could be substantiated with future work (Foreman et al., 2022; Finzel et al., 2023).

# **Tectonic linkages**

A two-phase system can explain the local tectonic cycles: (i) pulses of contraction and thrusting in the fold-and-thrust belt coupled with thrust-loading related sedimentation in the adjacent depocentres; and (ii) a lessening of thrust load due to relaxation in the fold-and-thrust belt which co-occurred with sedimentary reworking in the depocentre. The first tectonic cycle is preserved in the clast-rich Buckhorn Conglomerate, which would reflect thrust-loading in the adjacent foreland as a result of thrusting in the

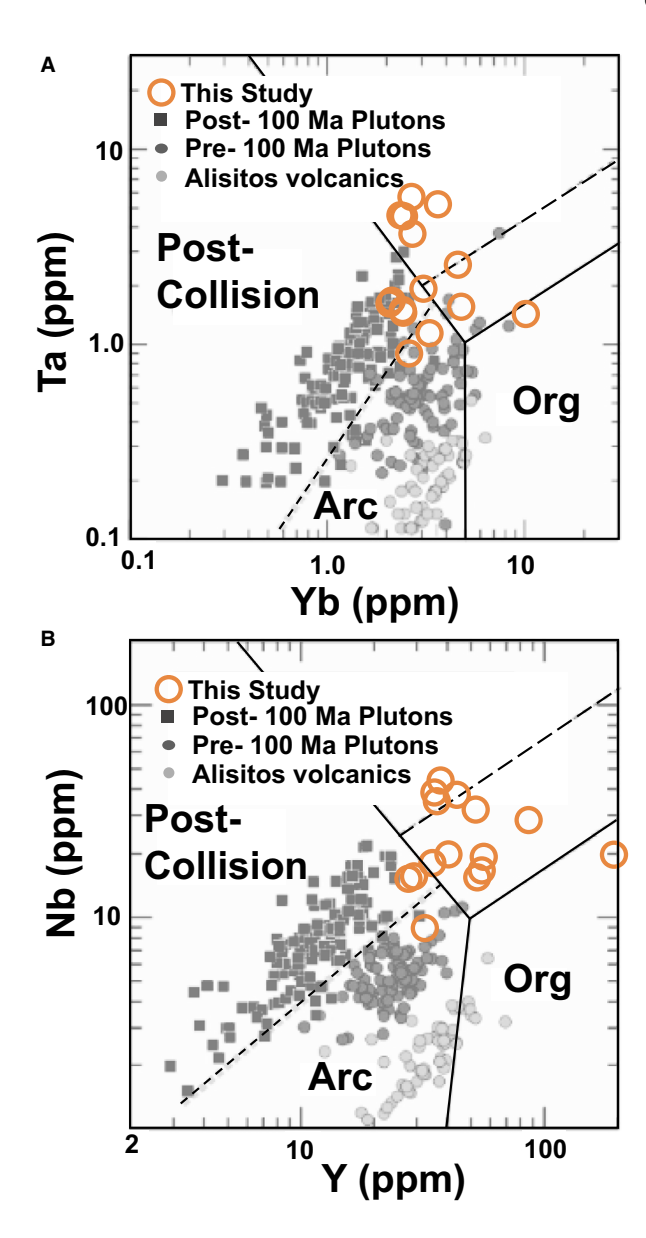


Fig. 14. Mussentuchit Ash Zones (Orange Circles) 1 to 4 plotted on two discrimination diagrams modified from Hildebrand *et al.* (2022, see fig. 27 therein). Historical data originally from Pearce *et al.* (1984) and Morris *et al.* (2019) shows that 130 to 100 Ma reflects Santiago Peak–Alisitos arc signatures and 100 to 86 Ma reflects Peninsular Range Batholith and the Alisitos volcanic arc.

Canyon Range (Lawton, 1986; Currie, 1997; Lawton et al., 2007; Stikes, 2007; Kirkland et al., 2016; Quick et al., 2020; Hildebrand et al., 2022). Subsequently, flexural rebound (erosion of thrust load) of the thrust belt would have resulted in a disconformity with overlying units and coincided with sediment reworking in the thrust-adjacent areas, including the Ruby Ranch floodplain-dominated depocentre (Fig. 9)

(Cardenas et al., 2020; Suarez et al., 2021a, 2021b). The above processes have primarily been placed temporally within the Aptian-Albian, with most recent ages placing the Ruby Ranch Member between 120 Ma and 110 Ma (Kirkland et al., 1997, 2016; Lawton et al., 2007; Ludvigson et al., 2010; Suarez et al., 2014; Tucker et al., 2020; Lee, 2021), synchronous with the shift from proximal forebulge sedimentation for the Ruby Ranch Member to Short Canyon and Mussentuchit members within the foredeep (Lawton et al., 2010; Ludvigson et al., 2010; Tucker et al., 2022). The shift from proximal forebulge to foredeep sedimentation would corroborate the interpreted sequence boundary suggested by Kirkland & Madsen (2007), Sprinkel et al. (2012) and Kirkland et al. (2016, and references therein). However, in the thrust adiacent foredeep, this boundary is demarcated by the Short Canvon Member, herein interpreted to be the end of the flexural rebound and rejuvenation of thrust-loading in the foredeep (Heller et al., 1988; Heller & Paola, 1989; Hunt et al., 2011; Kirkland et al., 2016; Quick et al., 2020).

The second cycle of thrusting locally is the linkage between the Pavant thrust and Short Canvon Member and the return of thrust loading. CA-ID-TIMS U-Pb dating of detrital zircons from the uppermost Short Canyon Member indicated an emplacement of clastics since 102.95  $\pm$  0.06 Ma (Figs 7 and 9), which is significantly older (ca 4 Myr) than the overlying Mussentuchit Member (Tucker et al., 2023), suggesting that this MDA likely significantly pre-dates deposition of the Short Canyon Member. Results from the Bayesian age modelling scenarios herein suggest that the Short Canyon Member was likely deposited closer to ca 100 Ma as there is no field evidence for a major disconformity (fifth to seventh-order bounding surface) between the Short Canvon Member and overlying Mussentuchit Member that would represent a long-lived hiatus (eighthorder) (for example, no significant downcutting) (Vail et al., 1977). This younger timing of deposition is consistent with the interpretation of Hunt et al. (2011) that the San Pitch Formation and the Canyon Range Conglomerate are incongruent (Hunt et al., 2011; Kirkland et al., 2016; Hildebrand et al., 2022, fig. 11, p. 13; Wink, 2022). As such, it is plausible that sediment unloading coupled with accommodation generated by renewed thrusting into the adjacent Short Canyon depocentre would have been contemporaneous with renewed thrusting in the westerly adjacent Pavant Thrust during the Albian-Cenomanian transition, which would be in agreement with age estimates of Pujols et al. (2020) and Quick et al. (2020). The interpretation herein is that the linkage of coeval thrusting and sedimentation between the Iron Springs thrust and the Marshall Creek debris flow may be reflected between the Pavant thrust, Canvon Range Conglomerate, with the Short Canyon Member as a distal portion of the alluvial complex. Although the timing constraints from Pujols et al. (2020) are for exhumation and not thrusting, the authors infer that the two are penecontemporaneous, reflected in increased sedimentation rates, following the interpretations of Gardner et al. (2022). If accurate, the Iron Springs and Pavant thrusts would be coeval with the Nebo thrust to the north, signifying that the responses to the Albian-Cenomanian tectonic transition is near-contemporaneous across much of Utah (DeCelles & Coogan, 2006; Bartnik, 2019; Schwartz et al., 2019, 2021; Lawton et al., 2020; Pujols et al., 2020; Quick et al., 2020; Chapman et al., 2021; Gardner et al., 2022; Hildebrand et al., 2022). In addition, this early phase of renewed thrusting and sediment unloading co-occurred with the regional TS2-SB3.1 transgression-regression or the KAI8 transgression-regression (Oboh-Ikuenobe et al., 2008; Haq, 2014; Miall & Catuneanu, 2019).

Following the deposition of the Short Canyon Member, flexural rebound occurred within the adjacent foredeep with the emplacement of the lower Mussentuchit Member. Sedimentation rates for the Mussentuchit Member are established to have been ca 8 m/Ma 99.494 + 0.063/-0.049 Ma (Figs 8 and 12C). During this period, the Mussentuchit depocentre was a landward paralic mudflat, forming a sink for suspension, settling fines with subsequent pedogenesis (Tucker et al., 2022, 2023). Deposition is contemporaneous with a minor transgression and a locally high base level just after the KAI8 regression and before the KCe1 regression and early phases of the TS3.1 (Oboh-Ikuenobe et al., 2008; Hag, 2014; Miall & Catuneanu, 2019; Tucker et al., 2023). Around 99.494 + 0.063/-0.049 Ma, subduction-related arc activity commenced, resulting contraction and increased thrusting rates in the Pavant that generated increased thrust loading and sedimentation between 99.494 + 0.063/-0.049 and 99.402 + 0.053/-0.066. Sedimentation rates likely increased with the emplacement of the last chance sandstone, which could account for the slightly higher apparent accumulation rate of ca 44 m/Ma in the lower Mussentuchit Member.

However, coeval with the last chance sandstone is a regional base-level fall in the Mussentuchit depocentres (Tucker *et al.*, 2022, 2023). This would corroborate early temporal estimations and linkages to the regional regression KCe1/SB3.2 by Oboh-Ikuenobe *et al.* (2008) and Haq (2014).

Sedimentary sequences overlying MAZ2 indicate slowing of sedimentation rate, with: interval (1) MAZ2 (99.402 + 0.053/-0.066 Ma) to MAZ3(99.193 + 0.054/-0.058 Ma)estimated 28.6 m/Ma; and interval (2) MAZ3 (99.193 + 0.054/ -0.058 Ma) to MAZ4 (98.878 + 0.160/-0.171 Ma) estimated at 12.7 m/Ma. During this time, the Mussentuchit depocentre was transitioning from a mixed process landward paralic zone into a distal floodplain with more influence by alluvial processes (Tucker et al., 2022). Besides minor channelization, most sediments are directly linked to ashfall accumulation or pedogenesis within a shortlived stable environment. This would have occurred with the ongoing base level fall and the SB3.2 regression (Oboh-Ikuenobe et al., 2008; Haq, 2014). As previously mentioned, MAZ4 at 98.878 + 0.160/-0.171 Ma indicated continued subduction-related volcanism in the arc, which resulted in thrusting/duplexing in the Pavant thrust that provided sediment into the foredeep. Although this is speculative, as the overlying Naturita Sandstone regionally erodes into the upper Mussentuchit Member (Garrison Jr. et al., 2007; Tucker et al., 2022, 2023), another erosive gravel lag separates the overlying Naturita Sandstone and the Tununk Shale (Eaton et al., 1990; Renaut et al., 2023). Throughout the study area, the uppermost bounding surface of the Mussentuchit Member was an erosive contact (fifth, sixth, or greater order) with downcutting by the overlying Naturita Sandstone. This study concurs with the definition of Young (1960, 1965), supported by Carpenter (2014), that the Naturita Sandstone correlates to the Dakota Sandstone. Distinguishing between the upper Mussentuchit and basal Naturita at a rough scale can become problematic due to: (i) variable amount of downcutting by the Naturita Formation; (ii) northward thinning of the Mussentuchit Member; and (iii) the lateral variability of sandstone and mudstone thickness between exposures in the Naturita Formation (ergo Phillips et al., 2021). However, field observations and newly obtained U-Pb age constraints indicate that these two sedimentary successions share a diachronous contact of  $\pm 3.0$  Ma or more (Tucker et al., 2020, 2023; Renaut et al., 2023). The authors also agree with Phillips et al. (2020) that the Naturita is an association of coastal and nearshore environments; however,

13653091, 0, Downloaded from https://onlinelibrary.wiley.com/doi/10.1111/sed.13211 by Stellenbosch University, Wiley Online Library on [04/07/2024]. See the Terms and Conditions (https://onlinelibrary.wiley.com/terms-and-conditions) on Wiley Online Library for rules of use; OA articles are governed by the applicable Creative Commons License

many outstanding complexities and different interpretations show the need for further chronostratigraphic ties and an improved framework (Phillips et al., 2021). This may also reflect bottom-up or top-down stratigraphy, as Kirkland et al. (2016) noted. Thus, the patterns of tightly linked volcanism, thrusting/contraction and sedimentation are interpreted to have continued to at least the Cenomanian-Turonian Boundary (Bhattacharya & MacEachern, 2009; Renaut et al., 2023). If substantiated, these multiple tectonic drivers could have contributed to ongoing regional mid-Cretaceous eurybatic fluctuations, OAE2 and the Cretaceous Thermal Maximum (Wang et al., 2014). Based on the above, the penecontemporaneous nature between the arc, thrust activity and sedimentation, as suggested by Pujols et al. (2020) and Quick et al. (2020), has been confirmed by this study. Lastly, this ca 2 Ma landscape evolution corroborates the analysis of Hildebrand & Whalen (2021b) and Hildebrand et al. (2022), which indicates that this is more contemporaneous with the Albian-Cenomanian Wrangellia accretion in southern Alaska than previously thought. Despite this, the resulting sedimentary influx into the adjacent foredeep was serendipitous to capture the influx of Asian dinosaurs and other exotic lineages.

# **Regional correlations**

Regional correlations across the Western Interior can be proposed or strengthened based on the aforementioned timeframe. To the north, and based on recent work by Gardner et al. (2022), the Pavant thrusting would be near-contemporaneous (ca 102 to 100 Ma) with thrust-unroofing in central Idaho and south-western Montana, namely the Pioneer and Hawley Creek thrust and progradation of the Blackleaf Formation D clastic wedge in Montana. If correct, this would corroborate that the Mussentuchit Member is penecontemporaneous with the Wayan Formation of eastern Idaho, based on the latter formation's depositional age of 101.4 to 97.55 Ma proposed by Dorr (1985) and Krumenacker et al. (2017). Recent geochronological results indicate an Albian (101.0 Ma) estimate for the lower Wayan Formation (Ross et al., 2017). Therefore, this study proposes a potential linkage between the lower Wayan Formation of Idaho and that of the Short Canyon Member (Krumenacker, 2019; Bonde et al., 2022). The Mussentuchit Member was emplaced penecontemporaneously with the Arrow Creek bentonite (Bootlegger Member) of the Blackleaf Formation D clastic wedge in south-western Montana (in

agreement with Gardner et al., 2022). This study agrees with the assertion of Gardner et al. (2022) that activity in the St. Mary and Hall Lake thrusts was likely near synchronous with thrusting in Utah. Corroboration of regional ties by Gardner et al. (2022) and others indicates that the Willard, Meade and Hawley Creek thrusts in northern Utah, Idaho and Wyoming are also penecontemporaneous to thrusting in central and southern Utah (Nebo, Pavant and Iron Springs thrusts) (Gentry et al., 2018; Craddock & Malone, 2022; Malone et al., 2022). This correlation could indicate a temporal linkage between the Short Canyon Member with the clastics in the western Bear River Formation (K3) and the Mussentuchit Member with the lower Aspen Formation (K4) (Ryer, 1994; Yonkee et al., 2019). Quick et al., 2020 (Fig. 9) proposed a correlation south of the Iron Springs thrust to the Keystone thrust system to ca 99 Ma, which this study agrees with based on the earlier work of Fleck & Carr (1990). Given an emplacement age between 99.494 (+0.063/-0.049) and 98.878 (+0.160/-0.171) Ma, the Mussentuchit Member would directly correlate to the late SB3.1-TS3.1-SB3.2 (Fig. 4), forming stronger linkages to the south with the uppermost Mesa Rica Sandstone and Romeroville Sandstone rather than the previously suggested Thatcher Limestone (Tucker et al., 2022). In closer geographic proximity, D'Emic et al. (2019) recently revised the temporal framework for the Cloverly Formation of Wyoming to between the Valanginian (140 Ma) to Cenomanian (98 Ma), via U-Pb LA-ICP-MS and CA-TIMS dating of detrital zircons. However, the lack of temporal constraint for the uppermost Himes Member and Greybull Sandstone (ca 109–98 Ma) precludes potential penecontemporaneous linkages with the Short Canyon and Mussentuchit members, in contrast to the proposed linkage with the underlying Ruby Ranch Member, suggested by Ludvigson et al. (2015) (D'Emic et al., 2019). It is also important to highlight the work of Foreman et al. (2022) that presents detrital zircon U-Pb ages for a key Cretaceous sedimentary succession in Wyoming. Based on the rough correlation, the upper Cedar Mountain Formation would be contemporaneous to: (i) the Bear River Formation, Aspen Shale of the Western Wyoming foredeep; and (ii) the very uppermost Thermopolis Shale and the lowermost parts of the Mowry Shale in the Bighorn Basin forebulge (based on table 1, p. 6 in Foreman et al., 2022).

To the south in Arizona and New Mexico, possible contemporaneous Albian–Cenomanian deposits include the Turney Ranch Formation, Cintura Formation, the upper Mojado Formation and the

Fig. 15. (A) Palaeogeographical reconstruction of Western North America, modified from Tucker *et al.* (2022); (B) lithostratigraphic intervals and Mussentuchit Ash Zones (MAZ) for the Cedar Mountain Formation, with the modified Bchron Bayesian age mode excluding MDA; (C) to (G) Facies reconstructions of the Short Canyon and Mussentuchit members corresponding to temporal placement on the Bchron Bayesian age mode (B).

13653091, 0, Downloaded from https://onlinelibrary.wiley.com/doi/10.1111/sed.13211 by Stellenbosch University, Wiley Online Library on [04/07/2024]. See the Terms and Conditions (https://onlinelibrary.wiley.com/terms-and-conditions) on Wiley Online Library for rules of use; OA articles are governed by the applicable Creative Commons. Licensea

13653091, 0, Downloaded from https://onlinelibrary.wiley.com/doi/10.1111/sed.13211 by Stellenbosch University, Wiley Online Library on [04/07/2024]. See the Terms and Conditions (https://onlinelibrary.wiley.com/rerms-and-conditions) on Wiley Online Library for rules of use; OA articles are governed by the applicable Creative Commons License

uppermost Beartooth Quartzite; however, these require further investigation (Clinkscales & Lawton, 2015; Amato, 2019; Ferguson et al., 2019; Lawton et al., 2020; Caylor et al., 2021). Also, correlations can be confirmed to the south between the Willow Tank Formation of southern Nevada and the Mussentuchit Member (Bonde et al., 2022). Lastly, although far from the study area, there are potential linkages to the Early—Late Cretaceous transition identified within the Kahiltna Basin, which contemporaneously experienced similar tectonic regimes (Hampton et al., 2010; Trop et al., 2020). The reader should note that many of these correlations remain inexact and are subject to refinement in future investigations.

# CONCLUSION

As a result of increased temporal resolution for the upper Cedar Mountain Formation in central Utah, meaningful tectono-sedimentary linkages across central Utah can now be established. Overall, the data obtained from this study support interpretations for reactivation of exhumation and erosion in the eastern front of the thrust belt across central Utah that occurred near-synchronously during the Albian-Cenomanian transition. This resulted in a series of orogen-transverse fluvial distributive fans that displaced sediments from the fold-and-thrust belt to the adjacent easterly foredeep, probably driven by arc-related volcanic processes and coeval crustal shortening. Although various local and regional studies have suggested many of the assertions mentioned above, the findings indicate that these events took place in a short geological timespan, roughly during the earliest Cenomanian (ca 100 Ma and ca 98.9 Ma). Therefore, sedimentation would have occurred simultaneously with ongoing tectonics. This study also found evidence that a late Early Cretaceous north-easterly flowing 'California Style' river had less influence on sedimentary processes and deposition in central Utah than in southern Utah, especially during the Albian-Cenomanian transition when it would have been all but absent. Lastly, these novel insights have strengthened regional linkages to key deposits across the Western Interior, and the importance of broadscale holistic studies has been highlighted. The tectonic and depositional events that occurred during the Early Cenomanian in Utah can be summarized as follows (Fig. 15A to G):

• Approximately 100.4 to ca 99.9 Ma (Fig. 9C): Reactivation of thrusting in the Iron Springs,

- Pavant and Nebo thrusts across Utah is in response to continental contraction related to subduction and volcanism in the Cordilleran Arc. Simultaneous erosion and transport of alluvial sediments into the adjacent foredeep, including the Short Canyon Member and the Marshall Creek fluvial debris flow, occurred. Specifically, the Short Canyon orogen—transverse distributive fluvial fans extend eastward across the depocentre, depositing coarse clastics that would mix with finer, more mature siliciclastics sourced from distal orogen—parallel fluvial influx via a developing late-Early Cretaceous north-easterly flowing "California Style" river.
- Approximately 99.9 to ca 99.4 Ma (Fig. 9D): Ongoing erosion of the Pavant thrust sedimentation into the adjacent foredeep with decreasing amounts of an orogen-parallel fluvial influx of sediments. Sedimentological allochthonous reconstruction for the adjacent Mussentuchit paralic depocentre is absent of fluvial sedimentation but rather is dominated by the accumulation of suspension settling fines, including ash from the first pulse of regional volcanism (MAZ1) along a mudflat. A minor influx of orogen-parallel sediment (suspension settling fines) was deposited into this depocentre, likely the distal influence of the interpreted Early Cretaceous northeasterly flowing 'California Style' river.
- Approximately 99.4 to ca 99.4 Ma (Fig. 9E): The first and second of four extensive ashfall deposits [Mussentuchit Ash Zones 1 and 2 (MAZ1 and MAZ2)] in the Mussentuchit Member suggest that volcanic activity increased during the earliest Cenomanian. Subduction and arc volcanism triggered simultaneous continental shortening and thrusting, resulting in coeval erosion into the adjacent foredeep between eruptions represented by the ashfall deposits MAZ1 and MAZ2. During this intra-volcanic phase, the last chance sandstone represents an orogen-transverse sandy debris flow beyond the intersection point of the alluvial fans to the west. After that, subsequent eruptions occurred at ca 99.402 Ma (MAZ2) and were coupled with an additional influx of alluvial-linked sedimentary sequences. These particular sediment successions would be contemporaneous to the Blackleaf Formation D clastic wedge, Bear River Formation and possibly the uppermost Cloverly Formation.
- Approximately 99.402 to ca 98.878 Ma and younger (Fig. 9F and G): Sedimentation accumulation in the Mussentuchit depocentre was tied to the ongoing erosion of the Pavant thrust; however, facies analysis indicates encroachment of distal

# 34 R. T. Tucker et al.

fluvial floodplain processes and not alluvial processes. This is speculative as Mussentuchit Ash Zone 4 (MAZ4) occurs near the disconformable contact with the overlying Naturita Sandstone, which exhibits local downcutting. However, it can be confidently noted that ongoing subduction triggered volcanism and continental contraction, resulting in thrusting coevally occurring with synchronous sediment emplacement into the foredeep well into the Cenomanian and likely the Turonian.

### **ACKNOWLEDGEMENTS**

We thank staff, students, and volunteers of the 2015 – 2022 expeditions for repeated explorations of the Mussentuchit Member; M. Leschin, S. Foss, G. McDonald, R. Anderson, R. Hunt-Foster, J. Kirkland, M. Hayden, J. Krishna, R. Irmis, P. Gensler, staff of the Price Field Office, the Bureau of Land Management, Utah State Office, Natural History Museum of Utah and Utah Geological Survey for permitting and expedition support. Financial support was provided by Stellenbosch University's Department of Earth Sciences, Stellenbosch, South Africa, North Carolina Museum of Natural Sciences, Canyonlands Natural History Association, Field Museum of Natural History, University of Minnesota, Stellenbosch University DRD and National Science Foundation awards FRES 1925973, 1925884. Any opinions, findings, conclusions, or recommendations expressed in this material are those of the authors and do not necessarily reflect the views of the National Science Foundation. Lastly, we wish to express our appreciation to Sedimentology Ed. G. Mangano, and AE T. Schwartz, along with reviewers T. Lawton and those who wished to remain anonymous; their comments and suggestions greatly improved previous versions of this manuscript.

# CONFLICT OF INTEREST

The authors declare that they have no known competing financial interests or personal relationships that could have appeared to influence the work reported in this paper.

### REFERENCES

Amato, J.M. (2019) Detrital zircon ages from Proterozoic, Paleozoic, and Cretaceous clastic strata in southern New Mexico, USA. Rocky Mt. Geol., 54, 19–32.

- Balgord, E.A., Yonkee, W.A., Wells, M.L., Gentry, A. and Laskowski, A.K. (2021) Arc tempos, tectonic styles, and sedimentation patterns during evolution of the North American Cordillera: Constraints from the retroarc detrital zircon archive. Earth Sci. Rev., 216, 103557.
- Barkat, R., Chakraborty, P.P., Saha, S. and Das, K. (2020) Alluvial architecture, paleohydrology and provenance tracking from the Neoproterozoic Banganapalle Formation, Kurnool Group, India: An example of continental sedimentation before land plants. *Precambrian Res.*, **350**, 105930.
- Bartnik, S.R. (2019) Provenance and Sediment Dispersal Trends from Lower-Upper Cretaceous Nonmarine Strata of the Cordilleran Foreland Basin in Northern New Mexico. Doctoral dissertation, pp. 1–24. New Mexico State University, Mexico.
- Benvenuti, M. and Martini, I.P. (2002) Analysis of terrestrial hyperconcentrated flows and their deposit. Flood and megaflood processes and deposits: recent and ancient examples. In: Flood and Megaflood Processes and Deposits (Eds Martini, I.P., Baker, V.R. and Garzón, G.), Int. Assoc. Sedimentol. Spec. Publ, 32, 167–193.
- Bhattacharya, J.P. and MacEachern, J.A. (2009) Hyperpycnal rivers and prodeltaic shelves in the Cretaceous seaway of North America. *J. Sediment. Res.*, **79**, 184–209.
- **Blakey, R.C.** (2014) Paleogeography and paleotectonics of the western interior seaway, Jurassic-Cretaceous of North America. *Search Discov.*, **72**, 30392.
- Bonde, J.W., Hall, R.L., Krumenacker, L.J. and Varricchio, D.J. (2022) Nevadadromeus schmitti (gen. et sp. nov.), a New Basal Neornithischian with Affinities to the Thescelosaurinae, from the Upper Cretaceous (Cenomanian) Willow Tank Formation of Southern Nevada. J. Ariz.-Nev. Acad. Sci., 50, 1–8.
- **Burnham, B.S.** and **Hodgetts, D.** (2018) Quantifying spatial and architectural relationships from fluvial outcrops. *Geosphere*, **15**, 1–18.
- Caldwell, W.G.E. (1984) Early Cretaceous transgressions and regressions in the southern interior plains. AAPG-CSPG Spec. Publ Mem., 9, 173–203.
- Cardenas, B.T., Mohrig, D., Goudge, T.A., Hughes, C.M., Levy, J.S., Swanson, T., Mason, J. and Zhao, F. (2020) The anatomy of exhumed river-channel belts: Bedform to beltscale river kinematics of the Ruby Ranch Member, Cretaceous Cedar Mountain Formation, Utah, USA. Sedimentology, 67, 3655–3682.
- Carpenter, K. (2014) Where the sea meets the land—the unresolved Dakota problem in Utah. *Utah Geol. Assoc. Pub.*, **43**, 357–372.
- Caylor, E.A., Carrapa, B., Sundell, K., DeCelles, P.G. and Smith, J.M. (2021) Age and deposition of the Fort Crittenden Formation: A window into Late Cretaceous Laramide and Cenozoic tectonics in southeastern Arizona. *Geol. Soc. Am. Bull.*, **133**, 1996–2016.
- Chapman, J.B., Shields, J.E., Ducea, M.N., Paterson, S.R., Attia, S. and Ardill, K.E. (2021) The causes of continental arc flare ups and drivers of episodic magmatic activity in Cordilleran orogenic systems. *Lithos*, **398**, 106307.
- Chen, L., Steel, R.J., Guo, F., Olariu, C. and Gong, C. (2017) Alluvial fan facies of the Yongchong Basin: Implications for tectonic and paleoclimatic changes during Late Cretaceous in SE China. J. Asian Earth Sci., 134, 37–54.
- Cifelli, R.L., Kirkland, J.I., Weil, A., Deino, A.L. and Kowallis, B.J. (1997) High-precision <sup>40</sup>Ar/<sup>39</sup>Ar geochronology and the advent of North America's Late

3653091, 0, Downloaded from https://onlinelibrary.wiley.com/doi/10.1111/sed.13211 by Stellenboseh University, Wiley Online Library on [04/07/2024]. See the Terms and Conditions (https://onlinelibrary.wiley.com/rerms-and-conditions) on Wiley Online Library for rules of use; OA articles are governed by the applicable Creative Commons

- Cretaceous terrestrial fauna. Proc. Natl. Acad. Sci. U. S. A., 94, 11163–11167.
- Cifelli, R.L., Nydam, R.L., Gardner, J.D., Weil, A., Eaton, J.G., Kirkland, J.I., Madsen, S.K. and Gillette, D.D. (1999) Medial Cretaceous vertebrates from the Cedar Mountain Formation, Emery County, Utah: the Mussentuchit local fauna. In: Vertebrate Fossils of Utah (Ed Gillette, D.D.), Utah Geol. Assoc, 20, 219–242.
- Clinkscales, C.A. and Lawton, T.F. (2015) Timing of Late Cretaceous shortening and basin development, Little Hatchet Mountains, southwestern New Mexico, USA—implications for regional Laramide tectonics. *Basin Res.*, 27, 453–472.
- Color, M. (2011) Geological Rock-Color Chart: With Genuine Munsell Color Chips. p. 9. Munsell Color, Grand Rapids, MI.
- Craddock, J.P. and Malone, D.H. (2022) An overview of strains in the Sevier thin-skinned thrust belt, Idaho and Wyoming, USA (latitude 42° N). In: Tectonic Evolution of the Sevier-Laramide Hinterland, Thrust Belt, and Foreland, and Postorogenic Slab Rollback (180–20 Ma) (Eds Craddock, J.P., Malone, D.H., Foreman, B.Z. and Konstantinou, A.), Geol. Soc. Am. Spec. Paper, 555, 133– 148.
- Crowley, J.L., Schoene, B. and Bowring, S.A. (2007) U-Pb dating of zircon in the Bishop Tuff at the millennial scale. *Geology*, **35**, 1123–1126.
- Currie, B.S. (1997) Sequence stratigraphy of nonmarine Jurassic-Cretaceous rocks, central Cordilleran forelandbasin system. Geol. Soc. Am. Bull., 109, 1206–1222.
- Currie, B.S. (2002) Structural configuration of the Early Cretaceous Cordilleran foreland-basin system and Sevier thrust belt, Utah and Colorado. J. Geol., 110, 697-718.
- D'Emic, M.D., Foreman, B., Jud, N.A., Britt, B.B., Schmitz, M. and Crowley, J.L. (2019) Chronostratigraphic revision of the Cloverly Formation (Lower Cretaceous, Western Interior, USA). Bull. Peabody Mus. Nat. Hist., 60, 3–40.
- DeCelles, P.G. (2004) Late Jurassic to Eocene evolution of the Cordilleran thrust belt and foreland basin system, western USA. Am. J. Sci., 304, 105–168.
- **DeCelles, P.G.** and **Coogan, J.C.** (2006) Regional structure and kinematic history of the Sevier Fold-and-Thrust Belt, central Utah. *Geol. Soc. Am. Bull.*, **118**, 841–864.
- DeCelles, P.G. and Graham, S.A. (2015) Cyclical processes in the North American Cordilleran orogenic system. *Geology*, **43**, 499–502.
- DeCelles, P.G., Lawton, T.F. and Mitra, G. (1995) Thrust timing, growth of structural culminations, and synorogenic sedimentation in the type Sevier orogenic belt, western United States. *Geology*, 23, 699–702.
- DeCelles, P.G., Ducea, M.N., Kapp, P. and Zandt, G. (2009) Cyclicity in Cordilleran orogenic systems. *Nat. Geosci.*, 2, 251–257.
- Di Fiori, R.V., Long, S.P., Fetrow, A.C., Snell, K.E., Bonde, J.W. and Vervoort, J. (2020) Syncontractional deposition of the cretaceous Newark canyon formation, diamond mountains, Nevada: Implications for strain partitioning within the US Cordillera. Geosphere, 16, 546–566.
- Dickinson, W.R. and Gehrels, G.E. (2008) Sediment delivery to the Cordilleran foreland basin: Insights from U-Pb ages of detrital zircons in Upper Jurassic and Cretaceous strata of the Colorado Plateau. Amer. J. Sci., 308, 1041–1082.
- Doelling, H.H. and Kuehne, P.A. (2013) Geologic map of the Short Canyon Quadrangle, Emery County, Utah: Utah Geological Survey. Map 255DM, scale 1:24,000, 13 pp.

- Doelling, H.H., Kuehne, P.A. and Kirkland, J.I. (2009) Geologic Map of the Willow Springs Quadrangle, Sevier and Emery Counties, Utah. *Utah Geo. Surv.*, 1–20.
- Dorr, J.A. (1985) Newfound Early Cretaceous dinosaurs and other fossils in southeastern Idaho and westernmost Wyoming. Contrib. Mus. Paleontol. Univ. Michigan, 27, 73–85.
- Eaton, J.G., Kirkland, J.I. and Kauffman, E.G. (1990) Evidence and dating of mid-Cretaceous tectonic activity in the San Rafael Swell, Emery County, Utah. Mt. Geol., 27, 39–45.
- Eberth, D.A., Britt, B.B., Scheetz, R., Stadtman, K.L. and Brinkman, D.B. (2006) Dalton Wells: Geology and significance of debris-flow-hosted dinosaur bonebeds in the Cedar Mountain Formation (Lower Cretaceous) of eastern Utah, USA. Palaeogeogr. Palaeoclimatol. Palaeoecol., 236, 217–245.
- Eggins, S. (2003) Laser ablation ICP-MS analysis of geological materials prepared as lithium borate glasses. *Geostand. Geoanal. Res.*, 27, 147–162.
- Elderbak, K., Leckie, R.M. and Tibert, N.E. (2014)
  Paleoenvironmental and paleoceanographic changes across
  the Cenomanian–Turonian Boundary Event (Oceanic
  Anoxic Event 2) as indicated by foraminiferal assemblages
  from the eastern margin of the Cretaceous Western Interior
  Sea. Palaeogeogr. Palaeoclimatol. Palaeoecol., 41, 29–48.
- Eldrett, J.S., Ma, C., Bergman, S.C., Lutz, B., Gregory, F.J., Dodsworth, P., Phipps, M., Hardas, P., Minisini, D., Ozkan, A. and Ramezani, J. (2015) An astronomically calibrated stratigraphy of the Cenomanian, Turonian and earliest Coniacian from the Cretaceous Western Interior Seaway, USA: Implications for global chronostratigraphy. Cretaceous Res., 56, 316–344.
- Ferguson, C.A., Youberg, A., Gilbert, W.G., Orr, T.R., Richard, S.M. and Spencer, J.E. (2019) Geologic Map of the Mount Fagan 7.5' Quadrangle, Eastern Pima County, Arizona: Arizona Geological Survey Digital Geologic Map DGM-11, version 2.0, map scale 1:24,000, 36 p.
- Fielding, C.R., Ashworth, P.J., Best, J.L., Prokocki, E.W. and Smith, G.H.S. (2012) Tributary, distributary and other fluvial patterns: What really represents the norm in the continental rock record? Sed. Geol., 261, 15–32.
- Finzel, E.S., Rosenblume, J.A., Pearson, D.M. and Zippi, P.A. (2023) Timing of the transition from Sevier- to Laramide-style tectonism in southwestern Montana based on the provenance of the Frontier Formation, North American Cordillera. *Tectonics*, 42, e2023TC007777.
- Fleck, R.J. and Carr, M.D. (1990) The age of the Keystone Thrust: laser-fusion <sup>40</sup>Ar/<sup>39</sup>Ar dating of foreland basin deposits, southern Spring Mountains, Nevada. *Tectonics*, 9, 467–476.
- Foreman, B.Z., Michael, D.D., Malone, D. and Craddock, J. (2022) Over-to under-to back-filled: Early evolution of the Sevier foreland basin in Wyoming, USA. In: Tectonic Evolution of the Sevier-Laramide Hinterland, Thrust Belt, and Foreland, and Postorogenic Slab Rollback (180–20 Ma) (Eds Craddock, J.P., Malone, D.H., Foreman, B.Z. and Konstantinou, A.), Geol. Soc. Am. Spec. Pap, 555, 67–99.
- Forster, C. (2022) Evaluation of Carbon Isotopic Chemostratigraphy of the Cedar Mountain Formation of Utah. Doctoral dissertation, p. 79. University of Arkansas, Fayetteville, AR.
- Gao, C., Ji, Y., Wu, C., Jin, J., Ren, Y., Yang, Z., Liu, D., Huan, Z., Duan, X. and Zhou, Y. (2020) Facies and depositional model of alluvial fan dominated by episodic flood events in arid conditions: An example from the

- - Poplar Quaternary Fan, north-western China. Sedimentology, 67, 1750-1796.
- Gardner, K. and Dorsey, R.J. (2021) Mixed carbonatesiliciclastic sedimentation at the margin of a late Miocene tidal strait, lower Colorado River Valley, south-western USA. Sedimentology, 68, 1893-1922.
- Gardner, C.T., Finzel, E.S., Rosenblume, J.A. and Pearson, D.M. (2022) Foreland basin response to middle Cretaceous thrust belt evolution, southwestern Montana, USA. Geosphere, 18, 1783-1803.
- Garrison, J.R., Jr., Brinkman, D., Nichols, D.J., Laver, P., Burge, D. and Thayn, D. (2007) A multidisciplinary study of the Lower Cretaceous Cedar Mountain Formation Mussentuchit Wash, Utah: a determination of the paleoenvironment and paleoecology of the Eolambia caroljonesa dinosaur quarry. Cretaceous Res., 28, 461-494.
- Gaschnig, R.M., Vervoort, J.D., Lewis, R.S. and Tikoff, B. (2011) Isotopic evolution of the Idaho batholith and Challis intrusive province, northern US Cordillera. J. Petrol., 52, 2397-2429.
- Gentry, A., Yonkee, W.A., Wells, M.L. and Balgord, E.A. (2018) Resolving the history of early fault slip and foreland basin evolution along the Wyoming salient of the Sevier Fold-and-Thrust Belt: Integrating detrital zircon geochronology, provenance modeling, and subsidence Tectonics, Sedimentary Basins, and analysis. In: Provenance: A Celebration of William R. Dickinson's Career (Eds Ingersoll, R.V., Lawton, T.F. and Graham, S.A.), Geol. Soc. Am. Spec. Paper, 540, 509-545.
- Giallorenzo, M.A., Wells, M.L., Yonkee, W.A., Stockli, D.F. and Wernicke, B.P. (2018) Timing of exhumation, Wheeler Pass thrust sheet, southern Nevada and California: Late Jurassic to middle Cretaceous evolution of the southern Sevier fold-andthrust belt. Geol. Soc. Am. Bull., 130, 558-579.
- Gradstein, F.M., Gradstein, F.P., Agterberg, J.G., Ogg, J., Hardenbol, P., Van Veen, J., Thierry, J. and Huang, Z. (1995) A Triassic, Jurassic and Cretaceous time scale. In: Geochronology, Time Scales and Global Stratigraphic Correlation (Eds Berggren, W.A., Kent, D.v., Aubry, M.P. and Hardenbol, J.), SEPM Spec. Publ, 54, 95-126.
- Gulbranson, E.L., Rasbury, E.T., Ludvigson, G.A., Möller, A., Henkes, G.A., Suarez, M.B., Northrup, P., Tappero, R.V., Maxson, J.A., Shapiro, R.S. and Wooton, K.M. (2022) U-Pb Geochronology and Stable Geochemistry of Terrestrial Carbonates, Lower Cretaceous Cedar Mountain Formation, Utah: Implications for Synchronicity of Terrestrial and Marine Carbon Isotope Excursions. Geosciences, 12, 346.
- Hampton, B.A., Ridgway, K.D. and Gehrels, G.E. (2010) A detrital record of Mesozoic Island arc accretion and exhumation in the North American Cordillera: U-Pb geochronology of the Kahiltna basin, southern Alaska. Tectonics, 29, TC4015.
- Haq, B.U. (2014) Cretaceous eustasy revisited. Global Planet. Change, 113, 44-58,
- Haslett, J. and Parnell, A. (2008) A simple monotone process with application to radiocarbon-dated depth chronologies. J. Roy. Stat. Soc. Ser. C: Appl. Stat., 57, 399-418.
- Heller, P.L. and Paola, C. (1989) The paradox of Lower Cretaceous gravels and the initiation of thrusting in the Sevier Orogenic Belt, United States Western Interior. Geol. Soc. Am. Bull., 101, 864-875.
- Heller, P.L., Angevine, C.L., Winslow, N.S. and Paola, C. (1988) Two-phase stratigraphic model of foreland-basin sequences. Geology, 16, 501-504.

- Herring, D.M., Greene, D.C., Comer, J.B., Inkenbrandt, P.C., Krahulec, K.A. and Pinnell, M.L. (2016) The western Utah thrust belt in the larger context of the Sevier Orogeny. Resources and geology of Utah's West Desert. Utah Geol. Assoc. Publ., 45, 131-146.
- Hildebrand, R.S. and Whalen, J.B. (2021a) The mid-Cretaceous Peninsular Ranges Orogeny: a new slant on Cordilleran tectonics? I: Mexico to Nevada. Can. J. Earth Sci., 58, 670-696.
- Hildebrand, R.S. and Whalen, J.B. (2021b) The mid-Cretaceous Peninsular Ranges Orogeny: a new slant on Cordilleran tectonics? II: northern United States and Canada. Can. J. Earth Sci., 58, 697-719.
- Hildebrand, R.S., Bhattacharva, J.P. and Whalen, J.B. (2022) The mid-Cretaceous Peninsular Ranges orogeny: a new slant on Cordilleran tectonics? III: The orogenic foredeep. Can. J. Earth Sci., **60**, 214–262.
- Hintze, L.F., Willis, G.C., Laes, D.Y., Sprinkel, D.A. and Brown, K.D. (2000) Digital geologic map of Utah:179DM, scale 1:500,000.
- Hong, H., Zhao, L., Fang, Q., Algeo, T.J., Wang, C., Yu, J., Gong, N., Yin, K. and Ji, K. (2019) Volcanic sources and diagenetic alteration of Permian-Triassic boundary Kbentonites in Guizhou Province, South China. Palaeogeogr. Palaeoclimatol. Palaeoecol., 519, 141-153.
- Huff, W.D. (2016) K-bentonites: A review. Am. Mineral., 101, 43 - 70.
- Hunt, G.J. (2015) U-Pb Detrital Zircon Geochronology of Lower Cretaceous Cedar Mountain and San Pitch Formations in Central-Eastern, Utah: A Record of Thrust Belt Unroofing. New Mexico State University, Mexico.
- Hunt, G.J., Lawton, T.F., Kirkland, J.I., Sprinkel, D.A., Yonkee, W.A. and Chidsey, T.C. (2011) Detrital zircon U-Pb geochronological provenance of Lower Cretaceous strata, foreland basin, Utah. Sevier Thrust Belt: Northern and Central Utah and Adjacent Areas. Utah Geol. Assoc. Publ., 40, 193–211.
- Jaffey, A.H., Flynn, K.F., Glendenin, L.E., Bentley, W.C. and Essling, A.M. (1971) Precision measurements of half-lives and specific activities of <sup>235</sup>U and <sup>238</sup>U. Phys. Rev. C, 4,
- Jochum, K.P., Weis, U., Stoll, B., Kuzmin, D., Yang, Q., Raczek, I., Jacob, D.E., Stracke, A., Birbaum, K., Frick, D.A. and Günther, D. (2011) Determination of Reference Values for NIST SRM 610-617 glasses following ISO Guidelines. Geostand. Geoanal. Res., 35, 397-429.
- Joeckel, R.M., Ludvigson, G.A., Möller, A., Hotton, C.L., Suarez, M.B., Suarez, C.A., Sames, B., Kirkland, J.I. and Hendrix, B. (2019) Chronostratigraphy and terrestrial palaeoclimatology of Berriasiane-Hauterivian strata of the Cedar Mountain Formation, Utah, USA. Geol. Soc. Spec. Pub., 498, 75-100.
- Johnstone, S.A., Schwartz, T.M. and Holm-Denoma, C.S. (2019) A stratigraphic approach to inferring depositional ages from detrital geochronology data. Front. Earth Sci., 7, 57.
- Keller, C.B., Schoene, B. and Samperton, K.M. (2018) A stochastic sampling approach to zircon eruption age interpretation. Geochem. Perspect. Lett., 8, 35.
- Kirkland, J.I. and Madsen, S.K. (2007) The Lower Cretaceous Cedar Mountain Formation eastern Utah: the view up an always interesting learning curve. (Field trip guide for 2007 Geol. Soc. Am. Field Trip Guidebook, Rocky Mountain Section, Annual Meeting, St. George, Utah, May 4-6, 2007). Utah Geol. Assoc. Publ., 35, 1-108.

13653091, 0, Downloaded from https://onlinelibrary.wiley.com/doi/10.1111/sed.13211 by Stellenbosch University, Wiley Online Library on [04/07/2024]. See the Terms and Conditions (https://onlinelibrary.wiley.com/rerms-and-conditions) on Wiley Online Library for rules of use; OA articles are governed by the applicable Creative Commons License

- Kirkland, J.I., Britt, B., Burge, D.L., Carpenter, K., Cifelli, R., DeCourten, F., Eaton, J., Hasiotis, S. and Lawson, T. (1997) Lower to middle Cretaceous dinosaur faunas: a key to understanding 35 million years of tectonics, evolution, and biogeography. Brigham Young Univ. Geol. Stud., 42, 69-103
- Kirkland, J.I., Cifelli, R., Britt, B.B., Burge, D.L., DeCourten, F., Eaton, J. and Parrish, J.M. (1999) Distribution of vertebrate faunas in the Cedar Mountain Formation, east-central Utah. In: Vertebrate Paleontology in Utah (Ed. Gillette, D.D.), Utah Geological Survey Miscellaneous Publication, 99, 201–217.
- Kirkland, J., Suarez, M., Suarez, C. and Hunt-Foster, R. (2016) The Lower Cretaceous in east-central Utah—the Cedar Mountain Formation and its bounding strata. Geol Intermountain West, 3, 101–228.
- Kleeberg, R., Monecke, T. and Hillier, S. (2008) Preferred orientation of mineral grains in sample mounts for quantitative XRD measurements: How random are powder samples? Clays Clay Miner., 56, 404–415.
- Krumenacker, L.J. (2019) Paleontological and chronostratigraphic correlations of the mid-Cretaceous Wayan-Vaughn depositional system of southwestern Montana and southeastern Idaho. *Hist. Biol.*, 31, 1301– 1311.
- Krumenacker, L.J., Simon, D.J., Scofield, G. and Varricchio, D.J. (2017) Theropod dinosaurs from the Albian– Cenomanian Wayan Formation of eastern Idaho. *Hist. Biol.*, 29, 170–186.
- Landing, E., Schmitz, M.D., Geyer, G., Trayler, R.B. and Bowring, S.A. (2021) Precise early Cambrian U-Pb zircon dates bracket the oldest trilobites and archaeocyaths in Moroccan West Gondwana. Geol. Mag., 158, 219–238.
- Laskowski, A.K., DeCelles, P.G. and Gehrels, G.E. (2013)
  Detrital zircon geochronology of Cordilleran retroarc foreland basin strata, western North America. *Tectonics*, 32, 1027–1048.
- Lawton, T.F. (1986) Compositional trends within a clastic wedge adjacent to a fold-thrust belt: Indianola Group, central Utah, USA. In: Foreland Basins (Eds Allen, P.A. and Homewood, P.), Int. Assoc. Sedimentol. Spec. Publ, 8, 411–423.
- Lawton, T.F., Sprinkel, D.A. and Waanders, G.L. (2007) The Cretaceous Canyon Range Conglomerate, central Utah stratigraphy, structure and significance. In: Central Utah— Diverse Geology of a Dynamic Landscape (Eds Willis, G.C., Hylland, M.D., Clark, D.L. and Chidsey, T.C., Jr.), Utah Geol. Assoc. Publ, 36, 101–122.
- Lawton, T.F., Hunt, G.J. and Gehrels, G.E. (2010) Detrital zircon record of thrust belt unroofing in Lower Cretaceous synorogenic conglomerates, central Utah. *Geology*, 38, 463–466.
- Lawton, T.F., Amato, J.M., Machin, S.E., Gilbert, J.C. and Lucas, S.G. (2020) Transition from Late Jurassic rifting to middle Cretaceous dynamic foreland, southwestern US and northwestern Mexico. Geol. Soc. Am. Bull., 132, 2489–2516.
- Lee, J. (2021) A Novel Approach to Date Continental Sediment Deposition and Paleoclimate Events Using Volcanogenic Zircon in Paleosols. Masters Degree Dissertation, p. 225. University of Kansas, Lawrence, KS.
- Li, S., Han, R., Du, Y., Liu, P. and Bie, H. (2020) Quantitative characterization of diagenetic reservoir facies of the Karamay alluvial fan in the Junggar Basin, western China. J. Petrol. Sci. Eng., 188, 106921.

- Lockshin, S.N., Yacobucci, M.M., Gorsevski, P. and Gregory, A. (2017) Spatial characterization of cretaceous Western Interior Seaway paleoceanography using foraminifera, fuzzy sets and Dempster-Shafer theory. Geo. Res. J., 14, 98–120. https://doi.org/10.1016/j.grj.2017.10.001
- Longerich, H.P., Jackson, S.J. and Günther, D. (1996) Laser ablation inductively coupled mass-spectrometric transient signal data acquisition and analyte concentration calculation. *J. Anal. At. Spectrom*, 11, 899–904.
- **Lowey**, **G.W**. (2023) The good, the bad, and the ugly: Analysis of three arguments in the ongoing debate concerning the polarity of Mesozoic arcs along the western margin of North America. *Geol. Soc. Am. Bull.*, **135**, 2591–2600.
- Ludvigson, G.A., Joeckel, R.M., Gonzalez, L.A., Gulbranson,
  E.L., Rasbury, E.T., Hunt, G.J., Kirkland, J.I. and Madsen,
  S. (2010) Correlation of Aptian-Albian carbon isotope excursions in continental strata of the Cretaceous foreland basin, eastern Utah, USA. J. Sediment. Res., 80, 955–974.
- Ludvigson, G.A., Joeckel, R.M., Murphy, L.R., Stockli, D.F., González, L.A., Suarez, C.A., Kirkland, J.I. and Al-Suwaidi, A. (2015) The emerging terrestrial record of Aptian-Albian global change. *Cretaceous Res.*, **56**, 1–24.
- Malone, D.H., Craddock, J.P. and Konstantinou, A. (2022)
  Timing and structural evolution of the Sevier thrust belt,
  western Wyoming. In: Tectonic Evolution of the SevierLaramide Hinterland, Thrust Belt, and Foreland, and
  Postorogenic Slab Rollback (180–20 Ma) (Eds Craddock,
  J.P., Malone, D.H., Foreman, B.Z. and Konstantinou, A.),
  Geol. Soc. Am. Spec. Pap, 555, 1–34.
- Mattinson, J.M. (2005) Zircon U-Pb chemical abrasion ("CA-TIMS") method: combined annealing and multi-step partial dissolution analysis for improved precision and accuracy of zircon ages. *Chem. Geol.*, **220**, 47–66.
- Miall, A.D. (2010) Alluvial Deposits. In: Facies Models 4 (Eds James, N.P. and Dalrymple, R.W.), Geol. Assoc. of Can. Geo, 20, 105–137.
- Miall, A.D. (2014) Fluvial depositional systems, p. 316. Springer International Publishing, Berlin.
- Miall, A.D. and Catuneanu, O. (2019) The Western Interior Basin. In: *The Sedimentary Basins of the United States* and Canada (Ed Miall, A.D.), 2nd edn, pp. 401–443. Elsevier B.V.
- Morris, R.A., DeBari, S.M., Busby, C., Medynski, S. and Jicha, B.R. (2019) Building arc crust: plutonic to volcanic connections in an extensional oceanic arc, the southern Alisitos arc, Baja California. *J. Petrol.*, **60**, 1195–1228.
- Neves, M.A., Morales, N. and Saad, A.R. (2005) Facies analysis of Tertiary alluvial fan deposits in the Jundiaí region, São Paulo, southeastern Brazil. *J. South Am. Earth Sci.*, **19**, 513–524.
- Nichols, G.J. and Fisher, J.A. (2007) Processes, facies and architecture of fluvial distributary system deposits. *Sed. Geol.*, **195**, 75–90.
- Norris, A. and Danyushevsky, L. (2018) Towards Estimating the Complete Uncertainty Budget of Quantified Results Measured by LA-ICP-MS. Goldschmidt Abstracts, Boston, MA.
- Oboh-Ikuenobe, F., Holbrook, J.M., Scott, R.W., Akins, S.L., Evetts, M.J., Benson, D.G. and Pratt, L.M. (2008) Anatomy of epicontinental flooding: Late Albian-Early Cenomanian of the southern US Western Interior Basin. *Geol. Assoc. Can. Spec. Pap.*, 48, 201–227.
- **Obradovich, J.D.** (1993) A Cretaceous time scale. In: Evolution of the Western Interior Basin (Eds Caldwell,

- W.G.E. and Kauffman, E.G.), Geol. Assoc. Can. Spec. Pap, 39, 379–396.
- Paterson, S.R. and Ducea, M.N. (2015) Arc magmatic tempos: Gathering the evidence. *Elements*, 11, 91–98.
- Pearce, J.A., Harris, N.B. and Tindle, A.G. (1984) Trace element discrimination diagrams for the tectonic interpretation of granitic rocks. J. Petrol., 25, 956–983.
- Peccerillo, A. and Taylor, S.R. (1976) Geochemistry of Eocene calc-alkaline volcanic rocks from the Kastamonu area, northern Turkey. *Contrib. Mineral. Petrol.*, **58**, 63–81.
- Phillips, S.P., Howell, J.A., Hartley, A.J. and Chmielewska, M. (2020) Tidal estuarine deposits of the transgressive Naturita Formation (Dakota Sandstone): San Rafael Swell, Utah, USA. J. Sediment. Res., 90, 777–795.
- Phillips, S.P., Howell, J.A., Hartley, A.J., Chmielewska, M. and Hudson, S.M. (2021) Evolution of foreland basin fluvial systems in the mid-Cretaceous of Utah, USA (upper Cedar Mountain and Naturita Formations). Sedimentology, 68, 2097–2124.
- Pujols, E.J., Stockli, D.F., Constenius, K.N. and Horton, B.K. (2020) Thermochronological and geochronological constraints on Late Cretaceous unroofing and proximal sedimentation in the Sevier orogenic belt, Utah. *Tectonics*, 39, e2019TC005794.
- Quick, J.D., Hogan, J.P., Wizevich, M., Obrist-Farner, J. and Crowley, J.L. (2020) Timing of deformation along the Iron Springs thrust, southern Sevier fold-and-thrust belt, Utah: Evidence for an extensive thrusting event in the mid-Cretaceous. Rocky Mt. Geol., 55, 75–89.
- R Core Team (2022) R: A Language and Environment for Statistical Computing. R Foundation for Statistical Computing, Vienna, Austria.
- Reading, H.G. (Ed) (2009) Sedimentary Environments: Processes, Facies and Stratigraphy, p. 704. John Wiley & Sons, Hoboken.
- Renaut, R.K., Tucker, R.T., King, M.R., Crowley, J.L., Hyland, E.G. and Zanno, L.E. (2023) Timing of the Greenhorn transgression and OAE2 in Central Utah using CA-TIMS U-Pb zircon dating. Cretaceous Res., 146, 105464.
- **Roberts, E.M.** (2007) Facies architecture and depositional environments of the Upper Cretaceous Kaiparowits Formation, southern Utah. *Sed. Geol.*, **197**, 207–233.
- Roca, X. and Nadon, G.C. (2007) Tectonic control on the sequence stratigraphy of nonmarine retroarc foreland basin fills: Insights from the Upper Jurassic of central Utah, USA. J. Sediment. Res., 77, 239–255.
- Ross, J.B., Ludvigson, G.A., Möller, A., Gonzalez, L.A. and Walker, J.D. (2017) Stable isotope paleohydrology and chemostratigraphy of the Albian Wayan Formation from the wedge-top depozone, North American Western Interior Basin. Sci. China Earth Sci., 60, 44–57.
- Ryer, T.A. (1994) Interplay of tectonics, eustacy, and sedimentation in the formation of mid-Cretaceous clastic wedges, Central and Northern Rocky Mountain regions. In: Unconformity Related Hydrocarbons in Sedimentary Sequences (Eds Dolson, J., Hendricks, M. and Westcott, W.), Rocky Mountain Association of Geologists Guidebook, 2, 35–44.
- Sambrook Smith, G.H., Best, J.L., Ashworth, P.J., Fielding, C.R., Goodbred, S.L. and Prokocki, E.W. (2010) Fluvial form in modern continental sedimentary basins: distributive fluvial systems: comment. *Geology*, **38**, 230.
- Schmitz, M.D. and Schoene, B. (2007) Derivation of isotope ratios, errors and error correlations for U-Pb geochronology

- using  $^{205}$ Pb- $^{235}$ U- $^{(233)}$ U)-spiked isotope dilution thermal ionization mass spectrometric data. *Geochem. Geophys. Geosyst.*, **8**, Q08006.
- Schwartz, T.M., Schwartz, R.K. and Weislogel, A.L. (2019) Orogenic recycling of detrital zircons characterizes age distributions of North American Cordilleran strata. *Tectonics*, 38, 4320–4334.
- Schwartz, T.M., Surpless, K.D., Colgan, J.P., Johnstone, S.A. and Holm-Denoma, C.S. (2021) Detrital zircon record of magmatism and sediment dispersal across the North American Cordilleran arc system (28–48° N). *Earth Sci. Rev.*, **220**, 103734.
- Shang, F., Chen, R., Zhao, Z., Scott, R.W. and Song, L. (2018) High-Precision Chronostratigraphic Correlation of Mid-Cretaceous Strata in Western Interior Basin, USA through Graphic Correlation Technique. GEP, 6, 266–277.
- Singer, B.S., Jicha, B.R., Sawyer, D., Walaszczyk, I., Buchwaldt, R. and Mutterlose, J. (2021) Geochronology of late Albian–Cenomanian strata in the US Western Interior. Geol. Soc. Am. Bull., 133, 1665–1678.
- Slattery, J.S., Cobban, W.A., McKinney, K.C., Harries, P.J. and Sandness, A.L. (2015) Early Cretaceous to Paleocene paleogeography of the Western Interior Seaway: the interaction of eustasy and tectonism. *Wyoming Geol. Surv. Guidebook*, **2**, 22–60.
- Sprinkel, D.A., Weiss, M.P., Fleming, R.W. and Waanders, G.L. (1999) Redefining the Lower Cretaceous stratigraphy within the central Utah foreland basin. *Utah Geol. Sur. Spec. Study*, **97**, 21.
- Sprinkel, D.A., Madsen, S.K., Kirkland, J.I., Waanders, G.L. and Hunt, G.I. (2012) Cedar Mountain and Dakota Formations around Dinosaur National Monument: Evidence of the incursion of the Cretaceous Western Interior Seaway into Utah. *Utah Geol. Sur. Spec. Study*, 143, 1–20.
- St. Pierre, G.A.E. and Johnson, C.L. (2022) Challenging assumptions of sediment routing in retroarc foreland basins: Detrital zircon evidence for axial versus transverse drainages in the Late Cretaceous of southern Utah, USA. *Basin Res.*, 34, 1960–1982.
- Stikes, M.W. (2007) Fluvial Facies and Architecture of the Poison Strip Sandstone Lower Cretaceous Cedar Mountain Formation, Grand County, Utah. Utah Geol. Sur., 6, 1–60.
- Stokes, W.L. (1952) Lower Cretaceous in Colorado Plateau. AAPG Bull., 36, 1766–1776.
- Suarez, C.A., González, L.A., Ludvigson, G.A., Cifelli, R.L. and Tremain, E. (2012) Water utilization of the Cretaceous Mussentuchit Member local vertebrate fauna, Cedar Mountain Formation, Utah, USA: using oxygen isotopic composition of phosphate. *Palaeogeogr. Palaeoclimatol. Palaeoecol.*, 313, 78–92.
- Suarez, C.A., González, L.A., Ludvigson, G.A., Kirkland, J.I., Cifelli, R.L. and Kohn, M.J. (2014) Multi-taxa isotopic investigation of paleohydrology in the Lower Cretaceous Cedar Mountain Formation, Eastern Utah, USA: deciphering effects of the Nevadaplano Plateau on regional climate. J. Sediment. Res., 84, 975–987.
- Suarez, M.B., Knight, J.A., Godet, A., Ludvigson, G.A., Snell, K.E., Murphy, L. and Kirkland, J.I. (2021a) Multiproxy strategy for determining palaeoclimate parameters in the Ruby Ranch Member of the Cedar Mountain Formation. Geol. Soc. Spec. Pub., 507, 313–334.
- Suarez, C.A., Frederickson, J., Cifelli, R.L., Pittman, J.G., Nydam, R.L., Hunt-Foster, R.K. and Morgan, K. (2021b) A new vertebrate fauna from the Lower Cretaceous Holly

13653091, 0, Downloaded from https://onlinelibrary.wiley.com/doi/10.1111/sed.13211 by Stellenbosch University, Wiley Online Library on [04/07/2024]. See the Terms and Conditions (https://onlinelibrary.wiley.com/rerms-and-conditions) on Wiley Online Library for rules of use; OA articles are governed by the applicable Creative Commons License

- Creek Formation of the Trinity Group, southwest Arkansas, USA. *PeerJ*, **9**, e12242.
- Suarez, M.B., Al Suwaidi, A., Montgomery, E.H., Kirkland, J.I., Andrew, J., Mclean, N., Möller, A., Ludvigson, G. and Suarez, C.A. (2023) New geochronological age constraint and chemostratigraphy for Aptian lacustrine strata, Cedar Mountain Formation, Utah. Geochem. Geophys. Geosyst., 24, e2023GC011014.
- Trayler, R.B., Schmitz, M.D., Cuitiño, J.I., Kohn, M.J., Bargo, M.S., Kay, R.F., Strömberg, C.A.E. and Vizcaíno, S.F. (2020) An improved approach to age-modeling in deep time: Implications for the Santa Cruz Formation, Argentina. Geol. Soc. Am. Bull., 132, 233–244.
- Trop, J.M., Benowitz, J.A., Koepp, D.Q., Sunderlin, D., Brueseke, M.E., Layer, P.W. and Fitzgerald, P.G. (2020) Stitch in the ditch: Nutzotin Mountains (Alaska) fluvial strata and a dike record ca. 117–114 Ma accretion of Wrangellia with western North America and initiation of the Totschunda fault. *Geosphere*, 16, 82–110.
- Tucker, R.T., Roberts, E.M., Darlington, V. and Salisbury, S.W. (2017) Investigating the stratigraphy and palaeoenvironments for a suite of newly discovered mid-Cretaceous vertebrate fossil-localities in the Winton Formation, Queensland, Australia. Sed. Geol., 358, 210–229.
- Tucker, R.T., Zanno, L.E., Huang, H.Q. and Makovicky, P.J. (2020) A refined temporal framework for newly discovered fossil assemblages of the upper Cedar Mountain Formation (Mussentuchit Member), Mussentuchit Wash, Central Utah. Cretaceous Res., 110, 104384.
- Tucker, R.T., Suarez, C.A., Makovicky, P.J. and Zanno, L.E. (2022) Paralic sedimentology of the Mussentuchit Member coastal plain, Cedar Mountain Formation, central Utah, USA. J. Sediment. Res., 92, 546–569.
- Tucker, R.T., Crowley, J.L., Mohr, M.T., Renaut, R.K., Makovicky, P.J. and Zanno, L.E. (2023) Exceptional age constraint on a fossiliferous sedimentary archive preceding the Cretaceous Thermal Maximum. Geology, 51, 962–967.
- Vail, P.R., Mitchum, R.M., Jr. and Thompson, S., III. (1977) Seismic stratigraphy and global changes of sea level: Part 4. Global cycles of relative changes of sea level.: Section 2. Application of seismic reflection configuration to stratigraphic interpretation, 83–97.
- Wang, Y., Huang, C., Sun, B., Quan, C., Wu, J. and Lin, Z. (2014) Paleo-CO<sub>2</sub> variation trends and the Cretaceous greenhouse climate. *Earth Sci. Rev.*, 129, 136–147.
- Weissmann, G.S., Hartley, A.J., Nichols, G.J., Scuderi, L.A., Olson, M., Buehler, H. and Banteah, R. (2010) Fluvial form in modern continental sedimentary basins: Distributive fluvial systems. *Geology*, **38**, 39–42.
- Willis, G.C. (1999) The Utah thrust system—an overview.
  In: Geology of Northern Utah and Vicinity (Eds Spangler, L.E. and Allen, C.J.), Utah Geol. Assoc. Publ,
  27. 1–9.
- Wink, J.T. (2022) Flexural Partitioning of the Later Albian-Cenomanian Cordilleran Foreland-Basin System, Utah, Wyoming, and Colorado. Doctoral dissertation. Miami University, Oxford, OH.

- Yingling, V.L. and Heller, P.L. (1992) Timing and record of foreland sedimentation during the initiation of the Sevier Orogenic Belt in central Utah. *Basin Res.*, 4, 279–290.
- Yonkee, W.A. and Weil, A.B. (2015) Tectonic evolution of the Sevier and Laramide belts within the North American Cordillera orogenic system. *Earth Sci. Rev.*, 150, 531–593.
- Yonkee, W.A., Eleogram, B., Wells, M.L., Stockli, D.F., Kelley, S. and Barber, D.E. (2019) Fault slip and exhumation history of the Willard Thrust Sheet, Sevier Fold-and-Thrust Belt, Utah: Relations to wedge propagation, hinterland uplift, and foreland basin sedimentation. *Tectonics*, 38, 2850–2893.
- Young, R.G. (1960) Dakota Group of Colorado Plateau. Bull. Am. Assoc. Pet. Geol., 44, 156–194.
- Young, R.G. (1965) Type section of the Naturita Formation. Bull. Am. Assoc. Pet. Geol., 49, 1512–1531.
- Yu, Z., Wang, Z., Fan, W., Wang, J. and Li, Z. (2022) Evaluating the sedimentological and diagenetic impacts on terrestrial lacustrine fan delta sandy conglomerates reservoir quality: Insights from the Triassic Baikouquan Formation in the Mahu sag, Junggar Basin, Western China. *Mar. Petrol. Geol.*, 146, 105973.
- Zanno, L.E., Tucker, R.T., Canoville, A., Avrahami, H.M., Gates, T.A. and Makovicky, P.J. (2019) Diminutive fleet-footed tyrannosauroid narrows the 70-million-year gap in the North American fossil record. *Commun. Biol.*, 2, 64.
- Zhang, Y., Colombera, L., Mountney, N.P., Gao, C., Ji, Y., Wu, H., Du, W., Liu, D., Bai, D. and Song, W. (2021) Sedimentation of open-framework gravels in alluvial-fan settings: Quaternary Poplar Fan, northwest China. Mar. Petrol. Geol., 134, 105376.

Manuscript received 30 November 2023; revision accepted 11 May 2024

# **Supporting Information**

Additional information may be found in the online version of this article:

**File S1** GPS locations for all samples used for the Short Canyon and Mussentuchit members, originally provided by Tucker *et al.* (2023).

**File S2** Cathodoluminescence images of zircon. Grains selected for CA-ID-TIMS are shown with analysis labels, as are locations of LA-ICP-MS spots with analysis labels.

File S3 LA-ICP-MS and CA-ID-TIMS methods in full.

File S4 LA-ICP-MS data in full.

File S5 CA-ID-TIMS data in full.